Research Square

Preprints are preliminary reports that have not undergone peer review.
They should not be considered conclusive, used to inform clinical practice,
or referenced by the media as validated information.

Thermo-Hydraulic Performance Comparison of Mono and Binary Hybrid Nanofluids in a Baffled Shell-and-Tube Heat Exchanger: A CFD Study

Md. Mehedi Hasan Sourobh
Khulna University of Engineering and Technology
Mohammad Sultan Mahmud
sultan@me.kuet.ac.bd

Khulna University of Engineering and Technology
Oliur Rahman
Khulna University of Engineering and Technology

Research Article

Keywords: Shell-and-tube heat exchanger, CFD, nanofluid, binary hybrid nanofluid, graphene nanoplatelets, pressure drop, thermal–hydraulic performance

Posted Date: November 24th, 2026

DOI: https://doi.org/10.21203/rs.3.rs-11436203/v1

License: This work is licensed under a Creative Commons Attribution 4.0 International License.
Read Full License

Additional Declarations: No competing interests reported.

Thermo-Hydraulic Performance Comparison of Mono and Binary Hybrid Nanofluids in a Baffled Shell-and-Tube Heat Exchanger: A CFD Study

Md. Mehedi Hasan Sourobh[1], Mohammad Sultan Mahmud[2*], and Oliur Rahman[3]

[1,2,3] *Department of Mechanical Engineering, Khulna University of Engineering & Technology (KUET), Khulna-9203, Bangladesh*

[1]mdmehedihasansourobh@gmail.com
[2]sultan@me.kuet.ac.bd (*Corresponding Author)
[3]oliur.mekuet@gmail.com

Abstract

A comparative thermo-hydraulic CFD investigation was conducted to evaluate the relative performance of water-based mono and binary hybrid nanofluids in a baffled shell-and-tube heat exchanger under identical geometrical and operating conditions.The single nanofluids studied were Al_2O_3/water, ZnO/water and graphene nanoplatelets (GNP)/water and the binary hybrid nanofluids were Al_2O_3–ZnO/water, Al_2O_3–GNP/water and ZnO–GNP/water. To make a consistent comparative assessment, all the working fluids were investigated under identical geometrical, boundary and numerical conditions. The simulations were conducted for different Reynolds numbers (10,000-25,000), different volume fraction of nanoparticles (1-5%) and different mass flow rates of shell side (0.5-2.0kg/s). A single-phase homogeneous flow model was used and the turbulent flow on the shell side was calculated by applying the realizable k–ε turbulence model. The numerical model was validated against benchmark shell-side data and the maximum deviations are obtained as 0.42%, 3.06%, 7.20% and 6.74%, respectively, for outlet temperature, pressure drop, heat-transfer rate and heat-transfer coefficient.The results show that with increase in Reynolds number/mass flow rate, the rate of heat transferred, heat transfer coefficient and average Nusselt number increases, and at the same time, pressure drop increases. The rate of heat transfer and the heat-transfer coefficient are enhanced by the increase in the nanoparticles volume fraction, but the average Nusselt number is found to decrease at a higher loading of nanoparticles as the increase of the effective thermal conductivity is more pronounced as compared to the heat-transfer coefficient increase in the Nusselt number expression. Among the single nanofluids, GNP/water achieved the highest heat-transfer-rate enhancement of 10.44% at ϕ = 5% compared

with pure water. In binary hybrid nanofluids, Al_2O_3–GNP/water demonstrated the maximum enhancement of 9.49% followed by ZnO–GNP/water and Al_2O_3–ZnO/water. Overall, GNP-containing fluids provide stronger heat-transfer enhancement, whereas ZnO/water and Al_2O_3–ZnO/water exhibit comparatively lower hydraulic resistance. These findings indicate that nanofluid selection for compact baffled shell-and-tube heat exchangers should be based on a balanced thermal–hydraulic assessment rather than heat-transfer enhancement alone

Keywords: Shell-and-tube heat exchanger; CFD; nanofluid; binary hybrid nanofluid; graphene nanoplatelets; pressure drop; thermal–hydraulic performance.

Nomenclature

Symbol	Description	Unit
A	Total heat-transfer area	m^2
B	Central baffle spacing	m
Bc	Baffle cut	%
C_p	Specific heat capacity	J kg^{-1} K^{-1}
D_h	Shell-side equivalent hydraulic diameter	m
D_s	Shell diameter	m
d_o	Tube outer diameter	m
d_r	Diameter ratio	–
f	Friction factor	–
h	Heat-transfer coefficient	W m^{-2} K^{-1}
k	Thermal conductivity	W m^{-1} K^{-1}
L	Heat-exchanger length	m
$\dot{m}$	Mass flow rate	kg s^{-1}
N	Number of baffles	–
N_t	Number of tubes	–
Nu	Nusselt number	–
P_t	Tube pitch	m
Q	Heat-transfer rate	W
Re	Reynolds number	–
T	Temperature	K

Symbol	Description	Unit
t	Time	s
u_i	Velocity component in the x_i direction	m s^{-1}
x_i	Spatial coordinate	m
ΔP	Pressure drop	Pa
ΔT_{lm}	Logarithmic mean temperature difference	K

Greek Symbols

Symbol	Description	Unit
α	Kinetic energy correction factor	–
ε	Turbulent dissipation rate	m^2 s^{-3}
ϕ	Nanoparticle volume fraction	%
μ	Dynamic viscosity	kg m^{-1} s^{-1}
μ_t	Turbulent viscosity	kg m^{-1} s^{-1}
ν	Kinematic viscosity	m^2 s^{-1}
ρ	Density	kg m^{-3}

Subscripts

Subscript	Description
bf	Base fluid
c	Cold fluid
h	Hot fluid
hnf	Hybrid nanofluid
i	Inlet
nf	Nanofluid
np	Nanoparticle
o	Outlet
$p1$	First nanoparticle
$p2$	Second nanoparticle
w	Water

Abbreviations

Abbreviation	Full form
Al_2O_3	Aluminum oxide
CFD	Computational fluid dynamics
CNT	Carbon nanotube
GNP	Graphene nanoplatelets
LMTD	Logarithmic mean temperature difference
MWCNT	Multi-walled carbon nanotube
STHE	Shell-and-tube heat exchanger
ZnO	Zinc oxide

1. Introduction:

Shell-and-tube heat exchangers (STHEs) are widely used in various industrial thermal systems, such as chemical and mechanical systems, heating and ventilation and conditioning systems, condensers, boilers, preheaters, fluid coolers, energy-generation systems, and applications of heat exchange in chemical processes, primarily due to their design flexibility, tubular construction, high-pressure capability, large heat-transfer surface area, and convenient cleaning and maintenance [1]. Recent design research also highlights the importance of considering heat duty, allowable pressure drop, operating uncertainty, process operability, and total cost in addition to the nominal heat-transfer performance in STHE optimization [2]. STHEs are also significant in waste heat recovery applications, where the unused thermal energy can be recovered from the system and to improve the thermal–hydraulic performance by having a better configuration of the exchanger [3]. However, performance improvement requires evaluation on improvements in heat transfer as well as pressure drop reduction since the hydraulic penalty will directly impact pumping power and thermal–hydraulic performance [1,4]. Thus, it is very meaningful in engineering to improve the STHE performance in order to decrease the size of equipment, energy consumption and operating cost of thermal systems in industries [1,2,4].

Baffles are routinely installed in shell-and-tube heat exchangers to direct the flow of fluids in the shell, to increase the contact area between the shell-side fluid and the tube bundle, to mix the fluids and to improve the shell-side convective heat transfer. Conventional segmental-baffle STHEs create the zigzag or cross-flow flow in the shell side, which may result in an increase in heat transfer rate but also in stagnant zones, tube-bundle vibration and relatively high pressure drop;

therefore, the heat transfer gain and pressure drop penalty must be considered together [5,6]. Recently, some investigations were carried out with modified baffle designs for further improvement of the overall thermal-hydraulic trade-off to reduce the pressure loss under an acceptable heat-transfer performance or to increase the comprehensive performance indices [4,6,7]. Hence, the performance of a baffled STHE will be judged based on the thermal–hydraulic performance with due regards to heat-transfer gain and pressure-drop/pumping-power penalty [4–6].

Although conventional heat-transfer fluids like water, ethylene glycol and thermal oils are readily available, they are compatible in operating conditions and have well-defined thermophysical behaviour, their thermal conductivity is relatively low which may limit the possible improvement in the rate of convective heat transfer in compact and high-duty thermal systems. Thus, nanofluids as engineered colloidal suspensions containing nanoscale metallic, metal-oxide or carbon based particles have been introduced to enhance the effective thermophysical properties of nanofluids such as thermal conductivity .Compared with pure base fluid, the addition of nanoparticles can increase the convective heat transfer due to the improvement in thermal energy transport and change in thermal transport behaviour, which depends on the type, size, shape, concentration of nanoparticles and the properties of the base fluid [8–10]. However, there are also significant practical limitations with nanofluid usage such as higher viscosity, particle agglomeration or sedimentation, long term stability issues, higher pressure drop and higher pumping-power requirement.Thus, nanofluids must not be judged only by their heat-transfer enhancement; their utility should be judged using a thermal–hydraulic point of view which considers the thermal gain in the balance of the hydraulic penalty [9–11].

The concept of hybrid nanofluids is an extension of the nanofluid concept, which involves mixing two types of nanoparticles with the same base fluid to produce synergised thermophysical properties.Their primary reason is that different classes of particles can overcome the drawbacks of each individual nanofluid, such as the practical stability of metal-oxide particles and the high intrinsic thermal conductivity of carbon-based particles like graphene nanoplatelets (GNPs), which also have an anisotropic morphology. Hybridization can create synergistic improvements in effective thermal conductivity and the convective heat-transfer performance relative to a single particle nanofluids, but the effect of these enhancements are highly dependent on nano-particle

pairing, mixing ratio, volume fraction, base fluid, Reynolds number, heat-exchanger geometry, and operating conditions [12–15]. Furthermore, if the proper combination of particles is not used or too many nanoparticles are added there is a risk of raising the viscosity, the tendency to agglomerate, the pressure drop, and the pumping-power. This can thus counteract the thermal gain. Hence, it is not possible to consider hybrid nanofluids as an ideal working fluid for all the applications and their performance must be evaluated based on thermal–hydraulic optimization between heat transfer improvement and hydraulic penalty [11,12,15].

Several experimental and numerical investigations have been carried out to investigate the performance of single-particle nanofluids for use as working fluids in STHEs in terms of convective heat-transfer performance, and taking into account the associated hydraulic penalty. Farajollahi et al. [16] studied the use of γ-Al_2O_3/water and TiO_2/water nanofluids in a STHE in the turbulent flow regime and concluded that the dispersion enhanced the convective heat-transfer behaviour. Lotfi et al. [17] investigated the MWNT/water nanofluid in a horizontal STHE and revealed that MWNT/water nanofluid can enhance the heat-transfer performance in the STHE compared with water. Ahmadi and Toghraie [18] numerically analyzed the CuO/water nanofluid in STHE and concluded that the heat transfer was enhanced with the addition of nanoparticles; however the friction factor was also increased. Heydari et al. [19] studied the effect of various types of nanofluids such as Fe, Fe_2O_3, Al_2O_3, Cu, CuO, SiO_2, Au in a small baffled STHE and found that the heat-transfer response was widely different depending on the type of nanoparticles and the base fluid. Hassaan [20] conducted an experimental study on MWCNT/water nanofluid in STHE and reported that heat-transfer coefficient, Nusselt number and effectiveness were significantly higher than distilled water especially at higher concentration of nanoparticles. Said et al. [21] investigated the performance of stable CuO/water nanofluid in a STHE and found that the convective heat-transfer coefficient and the overall heat-transfer performance of the nanofluid are improved. Somasekhar et al. [22] numerically investigated Al_2O_3/water nanofluid in a STHE and concluded that the heat transfer performance of nanofluid was improved as compared to distilled water. Kumar and Sonawane [23] investigated Fe_2O_3/water and Fe_2O_3/ethylene glycol nanofluids in a STHE where the effect of Reynolds number, nanoparticle concentration, type of base fluid and temperature on the heat-transfer enhancement were studied experimentally. Akhtari et al. [24] investigated and found that the α-Al_2O_3/water nanofluid behaviour was different in different heat exchanger configurations, namely in double pipe and shell-and-tube heat exchanger.

In general, it is observed from these studies that single nanofluids (metal-oxide, metallic and carbon-based) can be used to enhance the heat-transfer coefficient, Nusselt number, heat-transfer rate, and effectiveness in STHEs [16–24]. However, such enhancements are found to be particle-, concentration-, flow-, and geometry dependent and may be traded off with a corresponding increase in frictional resistance and pressure-drop penalty [18–20,23].

Further, based on the previous studies on mono-nanofluid, some studies have been recently investigated on binary hybrid nanofluid that uses complementary thermal and transport properties of two different nanoparticles in the same base fluid. Muneeshwaran et al. [25] discussed the enhancement of the heat-transfer characteristics of hybrid nanofluids and noted that the hybrid nanofluids can improve thermophysical properties and heat-transfer characteristics, considering the synthesis of nanoparticles, concentration, thermal conductivity, viscosity, Nusselt number, friction factor and the conditions of application. Vallejo et al. [26] made a critical comparison between the hybrid and mono nanofluids for convective heat transfer applications and found that it is not always better to use the hybrid nanofluids, as it depends on the flow regime, the type of heat transfer devices and the method of thermal–hydraulic evaluation. Moreover, Singh and Sood [27] carried out the review work of fabrication, thermophysical properties and applications of hybrid nanofluids, which are found to be the mixture of more than one nanoparticles for further enhancement of thermal properties, but while using hybrid nanofluids, it needs to be taken care of the methods of preparation, the composition of nanoparticles, and the prediction of properties. Rafid et al. [12] carried out a review on the recent uses of hybrid nanofluids in heat exchanger devices and mentioned that there are various challenges for the use of hybrid nanofluids in the heat exchanger such as stability, aggregation, thermal conductivity enhancement, fluid-flow characteristics, corrosion, material compatibility, cost, scalability, and environmental concerns. Malika et al. [28] studied experimentally and numerically the use of a hybrid nanofluid (CuO–ZnO/water) with low volume fraction in a STHE and found that the CuO–ZnO/water hybrid nanofluid leads to an improvement in both the heat-transfer coefficient and the Nusselt number, but the pressure drop is also increased. Behera et al. [29] have investigated the CuO–ZnO/water hybrid nanofluid in an STHE with circular, hexagonal and elliptical tube and concluded that CuO–ZnO/water hybrid nanofluid with elliptical tube shape has the significant effect on the heat-transfer rate, heat-transfer coefficient, Nusselt number and pressure drop. Shahsavar Goldanlou et al. [30] numerically investigated the performance of Fe_3O_4–CNT/water hybrid nanofluid in an STHE with

blade-shaped turbulators and found that the performance evaluation criterion was highly sensitive to Reynolds number, Fe_3O_4 concentration, CNT concentration, and blade-rod diameter. Alazwari and Safaei [31] studied the effect of different baffle angles on GNP–Ag/water hybrid nanofluid in an STHE and found that Nusselt number, pressure drop, friction factor and overall thermal performance were influenced by nanoparticle concentration, Reynolds number, and baffle arrangement. These studies show that the performance of heat exchanger can be improved by binary hybrid nanofluids; but, depending on the type of pairing of nanoparticles, concentration, stability, base fluid, Reynolds number, flow regime, and exchanger configuration, the efficiency of the binary hybrid nanofluids is also highly dependent [12,25–31].

Apart from working-fluid modification, the mixing of the shell-side, thermal boundary layer disturbance, and thermal–hydraulic performance improvement of STHEs have been extensively studied using baffle and/or geometry-assisted techniques. Alazwari and Safaei [31] demonstrated that the flow behaviour, temperature distribution, Nu, pressure drop and friction factor in an STHE with GNP–water hybrid nanofluid changed as function of the baffle angle and it was found that optimum angle of baffle for good thermal performance under their investigation was 135°. Shahsavar Goldanlou et al. [30] revealed that for the Fe_3O_4–CNT/water hybrid nanofluid, the blade-shaped turbulators can enhance the forced-convection heat transfer, while the optimum response is dependent on the Reynolds number, the nanoparticles loading, and the geometry of the turbulators. Bouselsal et al. [32] investigated Al_2O_3–MWCNT/water hybrid nanofluid in a tube/shell heat exchanger of various tube shapes and found that the concentration of the nanofluid, flow velocity and the tube shape has an influence on the rate of heat transfer, entropy generation and the Nusselt number with the enhancement of the performances being good for the diamond shape under the investigated conditions. Ghazanfari et al. [33] numerically investigated the simultaneous effect of twisted tubes and Al_2O_3 nanoparticles in an STHE and obtained that the concentration of Al_2O_3 nanoparticles can change the heat-transfer coefficient and pressure drop in addition to twisted tubes and a thermal–hydraulic evaluation is necessary. Mellal et al. [34] investigated the hydro-thermal performance on the shell side of the condenser with various baffle spacing and orientations and concluded that baffle orientation and spacing are significant parameters to control the pressure drop and to enhance the thermal performance. These studies collectively verify that hybrid nanofluids, baffle arrangement, blade-shaped turbulators, twisted tubes, and tube-shape modification can improve the performance of STHE; however, the

magnitude of the improvement is case dependent as different studies reported different sorts of hybrid nanofluids, different concentration, different Reynold number, different baffle arrangement and different tube shape, different boundary condition and different performance criteria [30–34].

Although significant research efforts have been devoted to improving the performance of shell-and-tube heat exchangers using mono nanofluids, hybrid nanofluids, and geometry modification techniques, a direct comparison of different working fluids remains challenging. Previous studies have generally investigated specific nanoparticle types, particular heat exchanger configurations, or different operating conditions, resulting in difficulties when comparing the reported thermal and hydraulic improvements among different studies. Moreover, although hybrid nanofluids have shown potential for enhancing heat transfer performance, their benefits are strongly dependent on nanoparticle combination, concentration, flow conditions, and the associated increase in hydraulic resistance. Therefore, a systematic assessment that simultaneously considers thermal enhancement and pressure-drop penalty under identical geometrical and operating conditions is still required.

In particular, the relative thermo-hydraulic performance of Al_2O_3/water, ZnO/water, GNP/water, Al_2O_3–ZnO/water, Al_2O_3–GNP/water, and ZnO–GNP/water nanofluids in a baffled shell-and-tube heat exchanger remains relatively less explored within a unified CFD framework.A controlled comparison using the same heat exchanger geometry, boundary conditions, numerical methodology, and operating range can provide a more reliable understanding of the advantages and limitations of different nanoparticle combinations.

Therefore, the present study investigates the thermal–hydraulic performance of water-based mono and binary hybrid nanofluids in a baffled compact shell-and-tube heat exchanger using a three-dimensional CFD approach. The effects of Reynolds number, nanoparticle volume fraction, and shell-side mass flow rate are evaluated in terms of outlet temperature, pressure drop, heat transfer rate, heat transfer coefficient, and average Nusselt number. The main contribution of this work is to establish a consistent comparison framework that identifies the trade-off between heat-transfer enhancement and hydraulic penalty among different nanofluid combinations under identical conditions. This approach provides practical insight into the selection of suitable working fluids for compact shell-and-tube heat exchanger applications.

2. Numerical Methodology

2.1 Geometrical configuration

A three-dimensional numerical model of the baffled shell-and-tube heat exchanger was created for the present CFD analysis. The heat exchanger is composed of a cylindrical shell, seven circular tubes, six segmental baffles, inlet and outlet for the shell side, and inlet and outlet for the tube side. The cold working fluid flows in through the shell-side inlet, out through the shell-side outlet, and the hot fluid flows through the tube side. The baffles help to direct the flow of the shell-side fluid across the tube bundle and improve fluid mixing. The layout of the main components of the heat exchanger and the flow directions are illustrated in a schematic representation in Fig. 1.

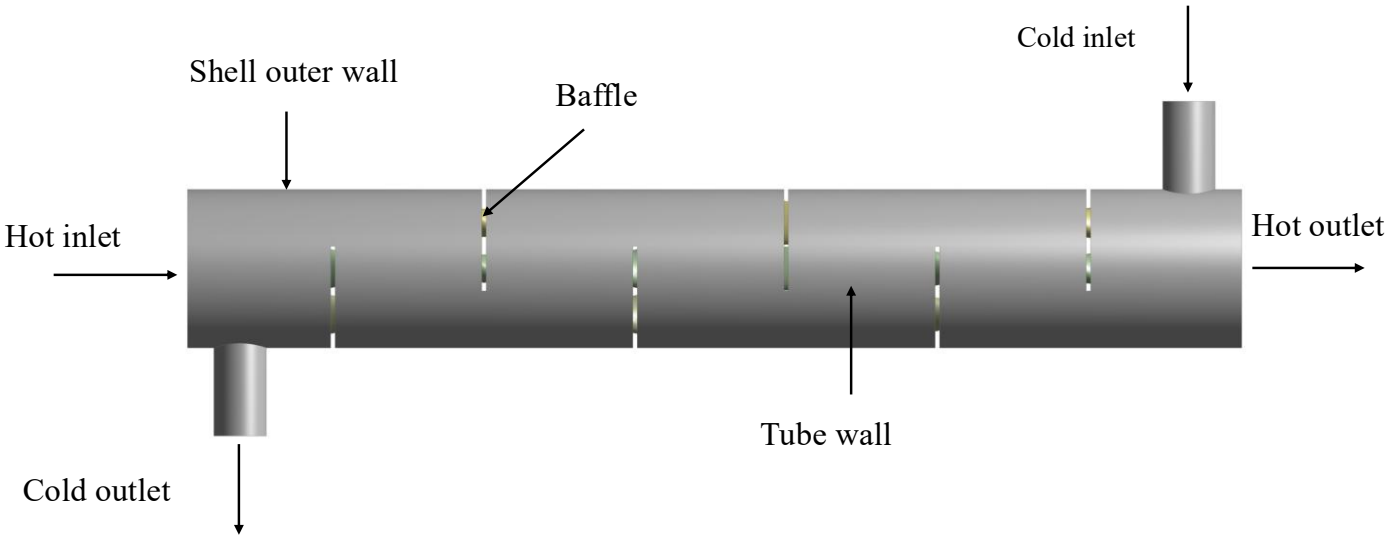

Fig.1. Schematic representation of a STHE, indicating the main components and the path of fluids.

Based on the schematic configuration, the computational geometry was created using ANSYS Design Modeler in ANSYS Workbench. The tube bundle was set in a triangular pitch, and the baffles were located in the length of the shell to create cross-flow on the shell side. To make a fair

comparison among water, single nanofluid, and hybrid nanofluid, the same geometrical model was used for all working fluids. The isometric view of the developed computational geometry is shown in Fig. 2.

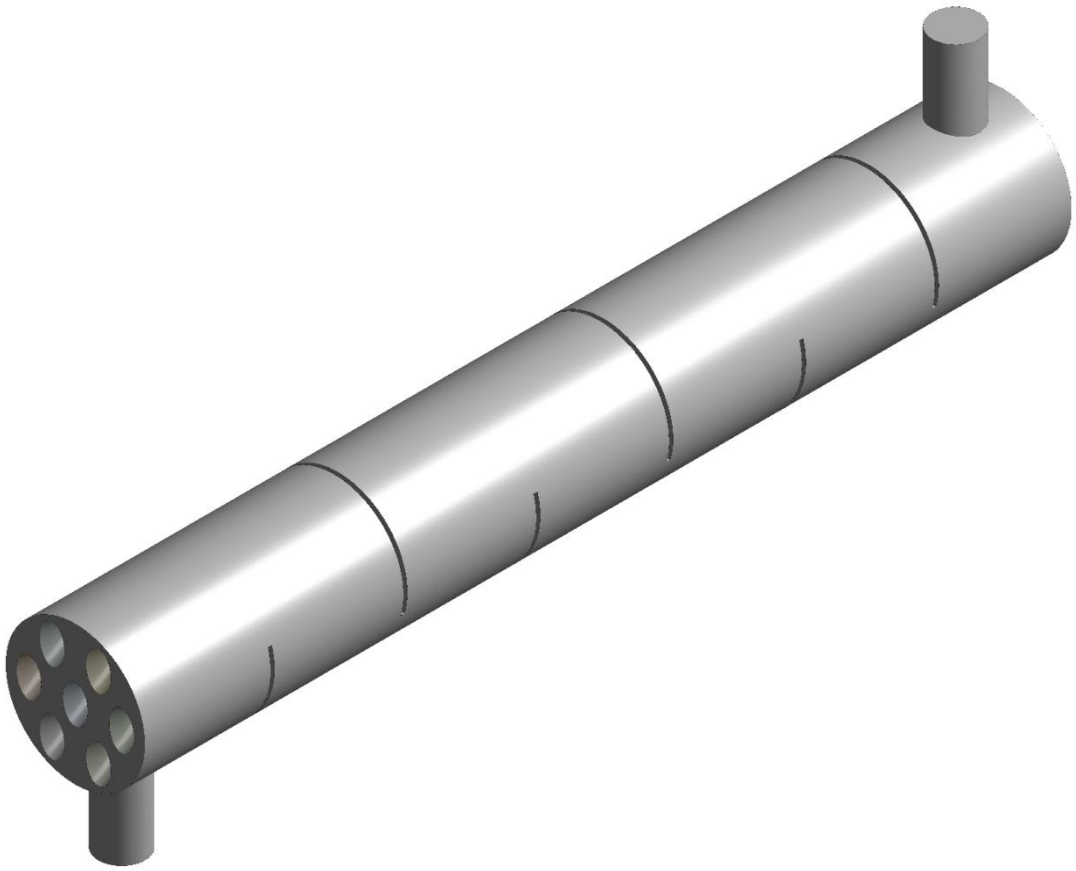

Fig. 2. Isometric view of the three-dimensional computational geometry of the baffled STHE.

The main geometrical parameters of the heat exchanger are summarized in Table 1. The geometry was chosen from the widely used reference model of the CFD analysis of the shell side of compact shell and tube heat exchangers proposed by Ozden and Tari [35].

Table 1
Geometrical parameters of the baffled shell-and-tube heat exchanger model.

Parameter	Value
Shell diameter, D_s	90 mm
Heat exchanger length, L	600 mm
Tube outer diameter, d_o	20 mm
Number of tubes, N_t	7
Tube configuration and pitch length, P_t	Triangular, 30 mm
Number of baffles, N_b	6
Central baffle spacing, B	86 mm
Baffle cut, B_c	36%

2.2 Modelling assumptions

Numerous assumptions were made in the current CFD model for the numerical analysis and computational nature. Table 2 summarizes these assumptions.

Table 2
Modelling assumptions used in the CFD simulation.

Category	Assumption
Flow condition	Steady, three-dimensional, turbulent, and incompressible flow
Nanofluid model	Single-phase homogeneous fluid model
Particle behaviour	Nanoparticles are uniformly dispersed in the base fluid
Slip condition	No relative slip between nanoparticles and base fluid
Thermal condition	Thermal equilibrium between nanoparticles and base fluid
Material properties	Thermophysical properties are constant for each simulation case

Neglected effects	Radiation, magnetic field, particle sedimentation, agglomeration, and chemical reaction are neglected

The nanofluids and hybrid nanofluids were assumed to be effective single phase fluids with equivalent thermophysical properties under assumptions as given in Table 2. In this way, the thermal-hydraulic performance of various working fluids can be compared using a common geometry, boundary conditions and numerical settings.

2.3 Numerical solution procedure

The numerical simulation were conducted on ANSYS Fluent software by finite volume method. A pressure-based steady-state solver was used to solve the governing equations of mass, momentum, and energy. Pressure-velocity coupling was done with the SIMPLE algorithm, and the gradient term was computed using the least-squares cell-based method. The pressure equation was discretized by the standard scheme and the momentum and energy equation were solved by the first-order upwind scheme. The realizable $k-\varepsilon$ turbulence model was chosen to model the turbulent shell-side flow induced by the baffles and the tube bundle.

Convergence criteria were taken as 10^{-6} for the energy equation, and 10^{-5} for the continuity, momentum and turbulence equations. To ensure that any differences in outlet temperature, pressure drop, heat transfer rate, heat transfer coefficient and Nusselt number between simulation cases were due to the working fluid type and the operating conditions, the same numerical settings were used for all simulation cases. The settings used in the numerical solver are summarized in Table 3.

Table 3
Numerical solver settings used in the CFD simulation.

Numerical parameter	**Setting**
CFD software	ANSYS Fluent
Solver type	Pressure-based, steady-state
Discretization method	Finite volume method
Pressure–velocity coupling	SIMPLE
Gradient evaluation	Least-squares cell-based

Pressure discretization	Standard
Momentum discretization	First-order upwind
Energy discretization	First-order upwind
Turbulence model	Realizable $k-\varepsilon$
Energy residual criterion	10^{-6}
Other residual criteria	10^{-5}

2.4 Governing Equations

ANSYS Fluent simulated the shell-side flow and heat transfer in the shell-and-tube heat exchanger by modeling using a three-dimensional, steady-state, incompressible, single-phase turbulent flow. The continuity, momentum and energy equations were also discretized and solved in the finite volume method to obtain the numerical formulation. The realizable k-ε model provided turbulence closure. The same equations have been commonly used in CFD simulations of shell-and-tube heat exchangers [4,6,36,37].

2.4.1 Continuity Equation

For steady incompressible flow, the continuity equation is written as:

$$\frac{\partial(\rho u_j)}{\partial x_j} = 0 \qquad (1)$$

where ρ is the fluid density and u_j is the velocity component in the x_j direction. Equation (1) represents conservation of mass throughout the computational domain.

2.4.2 Momentum Equation

The momentum conservation equation may be expressed as:

$$\frac{\partial(\rho u_i u_j)}{\partial x_j} = -\frac{\partial p}{\partial x_i} + \frac{\partial}{\partial x_j}\left[(\mu + \mu_t)\left(\frac{\partial u_i}{\partial x_j} + \frac{\partial u_j}{\partial x_i}\right)\right] \qquad (2)$$

where u_i and u_j are the velocity components in the x_i and x_j directions, respectively, p is the static pressure, μ is the molecular dynamic viscosity, and μ_t is the turbulent viscosity. This equation describes the balance among inertial, pressure and viscous/turbulent diffusion effects in the flow field.

2.3.3 Energy Equation

The energy conservation equation is given by,

$$\frac{\partial(u_j T)}{\partial x_j} = \frac{\partial}{\partial x_j}\left(\frac{\lambda}{\rho C_p}\frac{\partial T}{\partial x_i}\right) \tag{3}$$

where T is the fluid temperature, λ is the thermal conductivity, ρ is the fluid density, and C_p is the specific heat capacity at constant pressure. Equation (3) governs thermal energy transport through convection and diffusion within the fluid domain.

2.4.4 Realizable $k-\varepsilon$ turbulence model

To capture the complex turbulent shell-side flow, the realizable $\boldsymbol{k-\varepsilon}$ turbulence model was adopted. This model is suitable for flows involving streamline curvature, recirculation and complex secondary motion, and has been widely employed in CFD simulations of heat exchangers [37–39]

The transport equation for turbulent kinetic energy, k, is written as:

$$\frac{\partial}{\partial t}(\rho k) + \frac{\partial}{\partial x_j}(\rho k u_j) = \frac{\partial}{\partial x_j}\left[\left(\mu + \frac{\mu_t}{\sigma_k}\right)\frac{\partial k}{\partial x_j}\right] + G_k + G_b - \rho\varepsilon - Y_M + S_k \tag{4}$$

$$\frac{\partial}{\partial t}(\rho \varepsilon) + \frac{\partial}{\partial x_j}(\rho \varepsilon u_j) = \frac{\partial}{\partial x_j}\left[\left(\mu + \frac{\mu_t}{\sigma_\varepsilon}\right)\frac{\partial \varepsilon}{\partial x_j}\right] + \rho C_1 S\varepsilon - \rho C_2 \frac{\varepsilon^2}{k+\sqrt{\nu\varepsilon}} + C_{1\varepsilon}\frac{\varepsilon}{k}G_{3\varepsilon}G_b + S_\varepsilon \tag{5}$$

where,

$$C_1 = \max\left[0.43, \frac{\eta}{\eta+5}\right], \qquad \eta = S\frac{k}{\varepsilon}, \qquad S = \sqrt{2S_{ij}S_{ij}}$$

In equations (4) and (5), P_k denotes the production of turbulent kinetic energy due to the mean velocity gradients, whereas P_b represents the production of turbulent kinetic energy due to

buoyancy. The term Y_M accounts for the contribution of fluctuating dilatation in compressible turbulence to the total dissipation rate. S_k and S_ε are user-defined source terms, while σ_k and σ_ε are the turbulent Prandtl numbers for k and ε, respectively.

2.5 Properties of nanofluids and hybrid nanofluids

Table 4 lists the thermophysical characteristics of base fluids and nanoparticles. In this study, water based Al_2O_3, ZnO, GNP nanofluids and Al_2O_3-ZnO, Al_2O_3-GNP, ZnO-GNP hybrid nanofluids were employed for analysis of STHE.

Table 4

Thermophysical properties of water and nanoparticles [28, 40, 41]

	Density ρ (kg/m^3)	Specific Heat Cp (J/kgK)	Thermal Conductivity k (W/mK)
Water	997.1	4179	0.605
Al_2O_3	3970	765	40
ZnO	5600	860	29
Graphene (GNP)	2620	790	5300

2.6 Effective property models for nanofluids and hybrid nanofluids

The effective thermophysical properties of the nanofluids and hybrid nanofluids were calculated using standard mixture correlations at different nanoparticle volume fractions. The effective density of a single nanofluid is calculated as [42],

$$\mathrm{P_{nf}} = (1-\varphi)\rho_{\mathrm{bf}} + \varphi\rho_{\mathrm{np}} \tag{6}$$

The effective specific heat capacity of the nanofluid was calculated using the mixture heat-capacitance model as follows [42]:

$$C_{p_{nf}} = \frac{(1-\varphi)\rho_{\mathrm{bf}}\, C_{p_{bf}} + \varphi\rho_{\mathrm{np}} C_{p_{np}}}{(1-\varphi)\rho_{\mathrm{bf}} + \varphi\rho_{\mathrm{np}}} \tag{7}$$

The effective thermal conductivity of the nanofluid was calculated using the Maxwell-type relation derived from the Hamilton–Crosser effective-medium model [43],

$$k_{nf} = k_{bf}\left[\frac{k_p + 2k_{bf} + 2\varphi(k_p - k_{bf})}{k_p + 2k_{bf} - \varphi(k_p - k_{bf})}\right] \quad (8)$$

The dynamic viscosity of the nanofluid was estimated using the Batchelor correlation, which accounts for Brownian-motion effects in dilute particle suspensions [44]:

$$\mu_{nf} = (1 + 2.5\varphi + 6.5\varphi^2)\,\mu_{bf} \quad (9)$$

The effective thermophysical properties of the hybrid nanofluids were calculated using established mixture and effective-medium correlations. The total nanoparticle volume fraction was defined following the hybrid nanofluid formulation adopted by Takabi and Salehi [45]:

$$\phi = \phi_{p1} + \phi_{p2} \quad (10)$$

where ϕ is the total nanoparticle volume fraction, while ϕ_{p1} and ϕ_{p2} represent the volume fractions of the first and second nanoparticles, respectively.

The effective density of the hybrid nanofluid was calculated using the mixture relation commonly used for nanofluids and later adopted for hybrid nanofluids [45,46]:

$$\rho_{hnf} = \phi_{p1}\rho_{p1} + \phi_{p2}\rho_{p2} + (1 - \phi)\rho_{bf} \quad (11)$$

The effective specific heat capacity of the hybrid nanofluid was obtained from the weighted heat-capacity relation [45,46]:

$$C_{p,hnf} = \frac{\phi_{p1}\rho_{p1}C_{p,p1} + \phi_{p2}\rho_{p2}C_{p,p2} + (1-\phi)\rho_{bf}C_{p,bf}}{\rho_{hnf}} \quad (12)$$

The effective thermal conductivity of the hybrid nanofluid was estimated using the Hamilton–Crosser/Maxwell effective-medium approach as adopted in hybrid nanofluid modelling [43,45,47]:

$$k_{hnf} = k_{bf}\left[\frac{\frac{\phi_{p1}k_{p1} + \phi_{p2}k_{p2}}{\phi} + 2k_{bf} + 2(\phi_{p1}k_{p1} + \phi_{p2}k_{p2}) - 2\phi k_{bf}}{\frac{\phi_{p1}k_{p1} + \phi_{p2}k_{p2}}{\phi} + 2k_{bf} - (\phi_{p1}k_{p1} + \phi_{p2}k_{p2}) + \phi k_{bf}}\right] \quad (13)$$

The dynamic viscosity of the hybrid nanofluid was calculated using the Brinkman suspension model [45,48]:

$$\mu_{hnf} = \frac{\mu_{bf}}{(1-\phi)^{2.5}} \qquad (14)$$

In Eqs. (10)-(14), the subscripts bf, hnf, p1, and p2 denote the base fluid, hybrid nanofluid, first nanoparticle, and second nanoparticle, respectively. The symbols ρ, C_p, k, μ, and ϕ represent density, specific heat capacity, thermal conductivity, dynamic viscosity, and nanoparticle volume fraction, respectively.

2.7 Boundary and operating conditions

The boundary conditions were set based on the operating conditions of the baffled STHE. The shell-side inlet was specified as mass-flow inlet and the inlet temperature of the cold working fluid was kept at 300 K. The mass flow rate on the shell side was varied between 0.5 and 2.0 kg s^{-1} to evaluate the effect of flow rate on the thermal–hydraulic performance. The shell side outlet was taken as a pressure outlet with zero-gauge pressure. The heat transfer from the hot tube side to the cold shell-side working fluid was simulated by keeping the tube wall temperature constant at 450 K. The outer shell wall was assumed to be adiabatic with a zero-heat flux condition. All solid walls were treated as no-slip surfaces. The same boundary conditions were applied for water, single nanofluids and hybrid nanofluids, and the only parameters that different were working fluid properties, nanoparticle volume fraction and mass flow rate.

2.8 Mesh generation and mesh quality

ANSYS Meshing was used to discretize the computational domain. Due to the complex shell-side flow passage created by the tube bundle, baffles, inlet and outlet sections, an unstructured mesh was generated for the baffled shell-and-tube heat exchanger. To resolve the strong velocity and temperature gradients more accurately, local mesh refinement was performed near the tube surfaces, baffle edges, shell-side inlet and outlet regions. Inflation layers were also created near the wall regions to enhance the near wall flow and thermal boundary layer resolution. The details of the generated mesh are shown in Fig. 3.

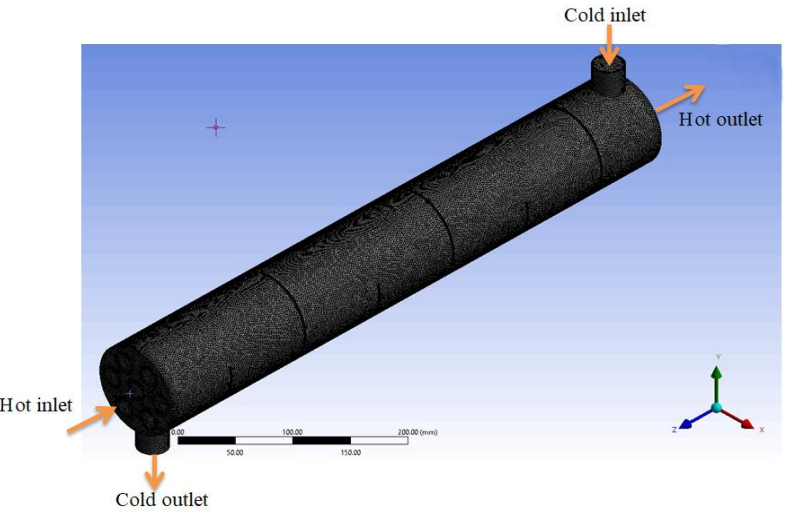

(a)

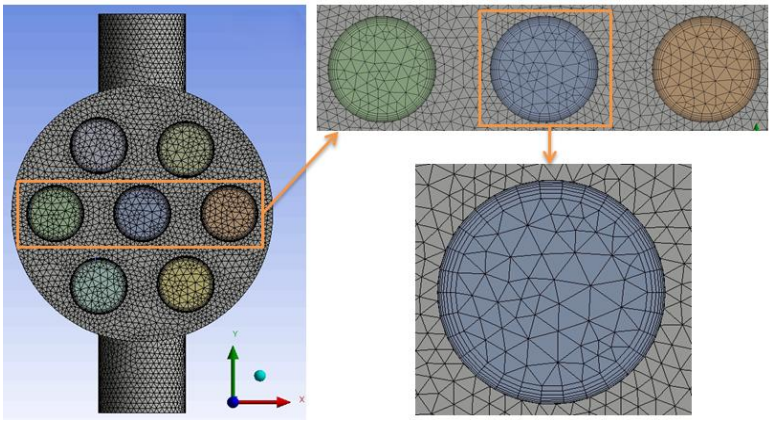

(b)

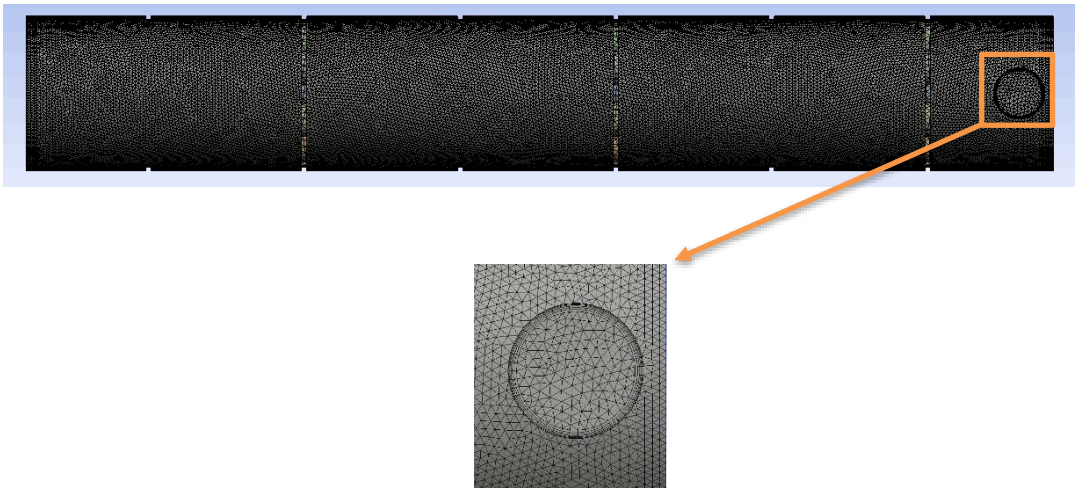

(c)

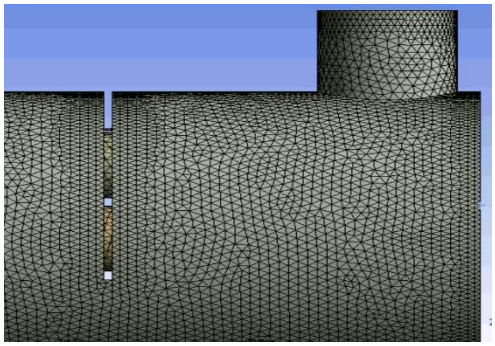

(d)

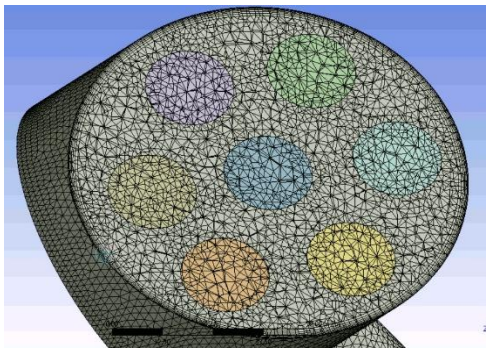

(e)

Fig. 3. Computational mesh of the baffled shell-and-tube heat exchanger: (a) overall isometric mesh, (b) local mesh refinement near the tube inlet region, (c) mesh refinement near the shell-side inlet region, (d) edge sizing near the baffle and wall regions, and (e) sectional mesh view of the tube bundle.

The mesh was enhanced in the vicinity of the tube bundle and baffle regions since these areas have a strong influence on the shell-side cross flow, recirculation and heat transfer features. The sectional mesh view shows that proper refinement has been done around the tubes and in the shell side flow passage. Table 5 gives a summary of the main mesh quality parameters.

Table 5
Mesh quality parameters of the computational domain.

Mesh parameter	**Value**
Mesh element size	2.1 mm
Growth rate	1.2
Number of elements	1,698,658
Average orthogonal quality	0.7932
Average skewness	0.20488

The average orthogonal quality of 0.7932 and the average skewness of 0.20488 show that the created mesh is good enough for the current CFD simulation. Before the full set of numerical simulations were performed, the selected mesh was further evaluated by performing a grid independence test.

2.9 Grid independence test

A grid independence test was conducted to make sure no appreciable effect on the numerical results was observed due to the grid resolution. The shell-side outlet temperature was chosen as the monitoring parameter in several mesh systems which were generated by increasing gradually the number of elements. The variation of outlet temperature with number of mesh elements is presented in Fig. 4.

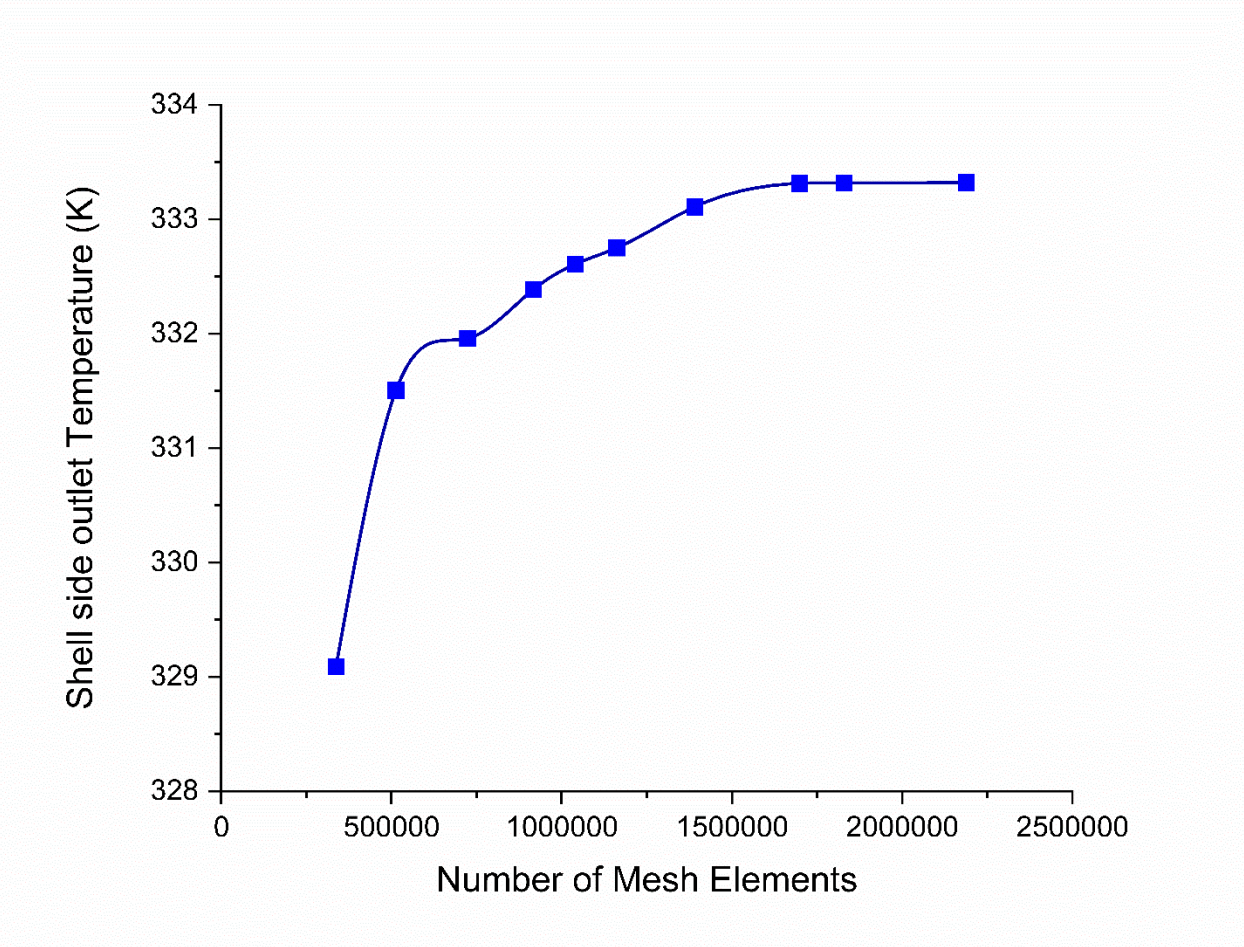

Fig. 4. Grid independence test based on shell-side outlet temperature for different mesh sizes.

This shell side outlet temperature was slowly stabilized with increasing number of elements. The outlet temperature in using 1,698,658 elements was 333.331K, however when the number of elements was increased to 1,828,321 and 2,188,384 elements, the outlet temperature was 333.354K

and 333.342K, respectively. The variation between two adjacent meshes was negligible after 1,698,658 elements and thus this mesh was chosen for the last simulations to ensure a numerical accuracy that was commensurate with the amount of computing effort required.

2.10 Data reduction and performance parameters

The CFD-predicted temperature, pressure and velocity field in the baffled shell and tube heat exchanger were used to assess its thermal–hydraulic performance. The heat transfer rate was determined based on the energy balance of the working fluid. The rate of heat transfer for a conventional heat exchanger is given by:

$$\dot{Q} = \dot{m}_h C_{p,h}(T_{h,in} - T_{h,out}) = \dot{m}_c C_{p,c}(T_{c,out} - T_{c,in}) \qquad (15)$$

where the subscripts h, c, inand outdenote hot fluid, cold fluid, inlet and outlet, respectively. The tube wall was considered a constant temperature and the rate of heat transfer was calculated from the shell side cold working fluid in the present CFD model.

The average value of the heat transfer coefficient was determined as:

$$h_{avg} = \frac{\dot{Q}}{A\Delta T_m} \qquad (16)$$

where A is the total heat transfer area and ΔT_m is the logarithmic mean temperature difference between the constant tube wall and the shell-side working fluid. The logarithmic mean temperature difference was calculated as

$$\Delta T_m = \frac{(T_w - T_{c,in}) - (T_w - T_{c,out})}{\ln\left(\frac{T_w - T_{c,in}}{T_w - T_{c,out}}\right)} \qquad (17)$$

where $T_w$is the constant tube wall temperature.

The shell-side equivalent hydraulic diameter was calculated using

$$D_e = \frac{4(P_t^2 - 0.25\pi d_o^2)}{\pi d_o} \qquad (18)$$

where $P_t$is the tube pitch and $d_o$is the tube outer diameter. The Reynolds number was calculated as

$$Re = \frac{\rho v D_e}{\mu} \qquad (19)$$

where ρ, v, $D_e$and $\mu$are the density, average velocity, equivalent hydraulic diameter and dynamic viscosity of the working fluid, respectively.

The shell-side pressure drop was obtained from the difference between the area-weighted average pressures at the shell-side inlet and outlet:

$$\Delta P = P_{in} - P_{out} \qquad (20)$$

The friction factor was calculated as

$$f = \frac{2\Delta P D_e}{\rho v^2 L} \qquad (21)$$

where $L$is the heat exchanger length. The average Nusselt number was determined from

$$Nu = \frac{h_{avg} D_e}{k} \qquad (22)$$

where $k$is the thermal conductivity of the working fluid.

The heat transfer enhancement relative to the base fluid was calculated as

$$\eta_Q = \frac{\dot{Q}_{nf/hnf} - \dot{Q}_{bf}}{\dot{Q}_{bf}} \times 100 \qquad (23)$$

where the subscripts $nf/hnf$and bfindicate nanofluid or hybrid nanofluid and base fluid, respectively.

Where, k represents the working fluid's thermal conductivity.

2.11 Model validation

The validation of the current CFD model was done with the benchmark shell-side numerical results of Ozden and Tari [35]. The same baffled shell and tube heat exchanger configuration was used for the validation with water as working fluid. Three different shell side mass flow rates of 0.5 kg/s, 1.0 kg/s and 2.0kg/s were investigated. A comparison was made for four important thermal–hydraulic parameters such as the shell outlet temperature, shell pressure drop, total heat transfer

rate and heat transfer coefficient.It is observed that, as presented in Fig. 5, the present CFD results are in good agreement with the benchmark results in the investigated mass-flow-rate range. The maximum deviation of the model outlet temperature of the shell side was predicted to be only 0.42% which shows good thermal response of the model. There was also a good agreement for the shell side pressure drop with the maximum deviation being 3.06%. The maximum deviations occurred in the total heat-transfer rate and heat-transfer coefficient, which were 7.20% and 6.74%, respectively. These deviations are acceptable for CFD simulation of baffled shell-side flow in which cross-flow, baffle-induced recirculation, secondary motion, flow separation and near wall thermal gradients strongly influence the numerical solution.The validation also shows that the present model is successful in capturing the overall thermal–hydraulic trends mentioned in the reference study. As the mass flow rate increases, the shell-side pressure drop, total heat-transfer rate and heat-transfer coefficient increases, and the shell-side outlet temperature shows the same general trend as the benchmark data. The slight differences between the present results and the reference data may be related to the difference in mesh resolution, discretisation scheme, solver setting, and treatment of thermophysical properties. Based on this, the adopted geometry, boundary conditions, turbulence model, mesh strategy and numerical solution procedure were found reliable for the following simulations with mono and binary hybrid nanofluids.

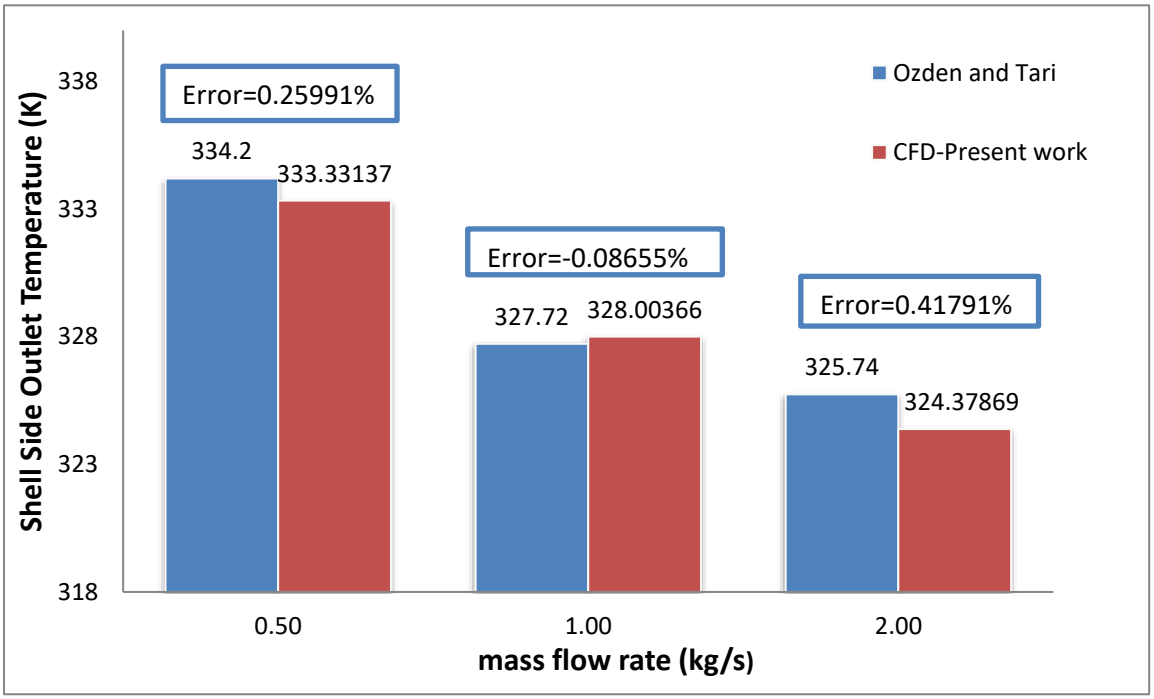

(a)

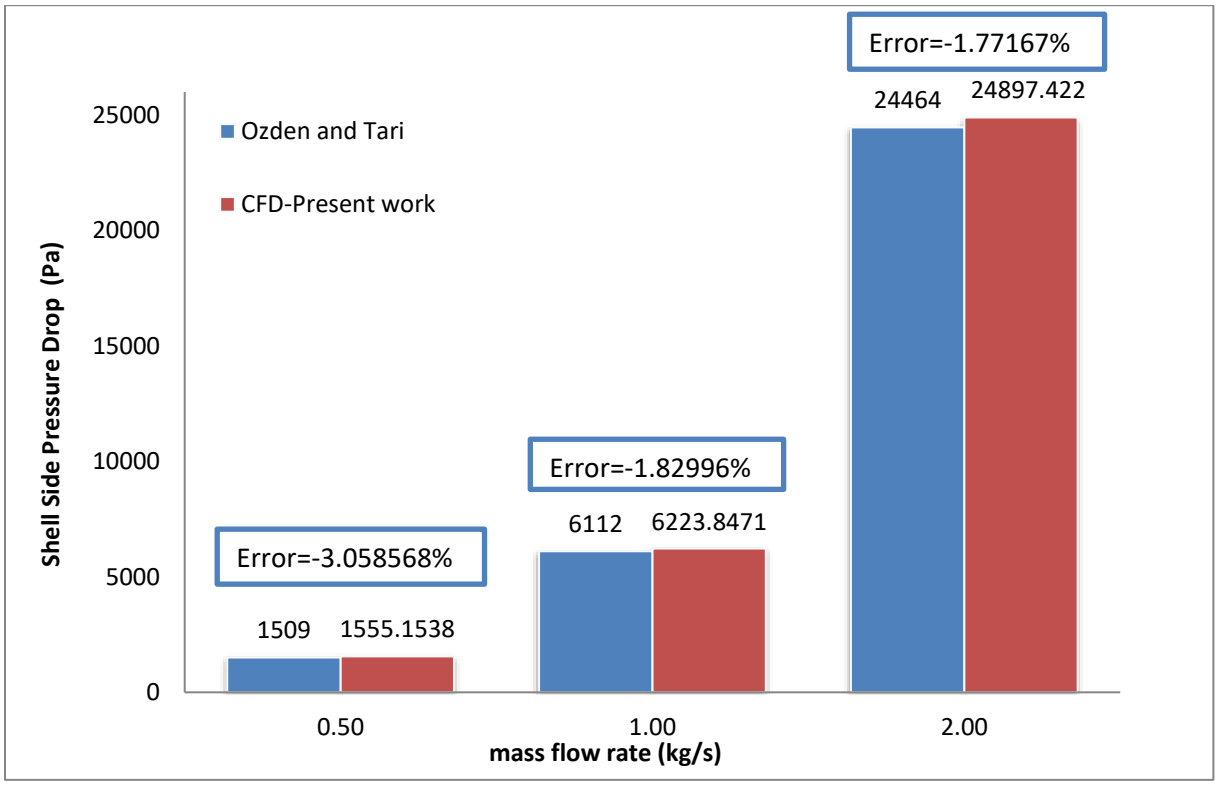
Error=-1.77167%
24464
24897.422
Ozden and Tari
CFD-Present work
25000
20000
15000
10000
5000
0
Shell Side Pressure Drop (Pa)
Error=-1.82996%
6112
6223.8471
Error=-3.058568%
1509
1555.1538
0.50
1.00
2.00
mass flow rate (kg/s)

(b)

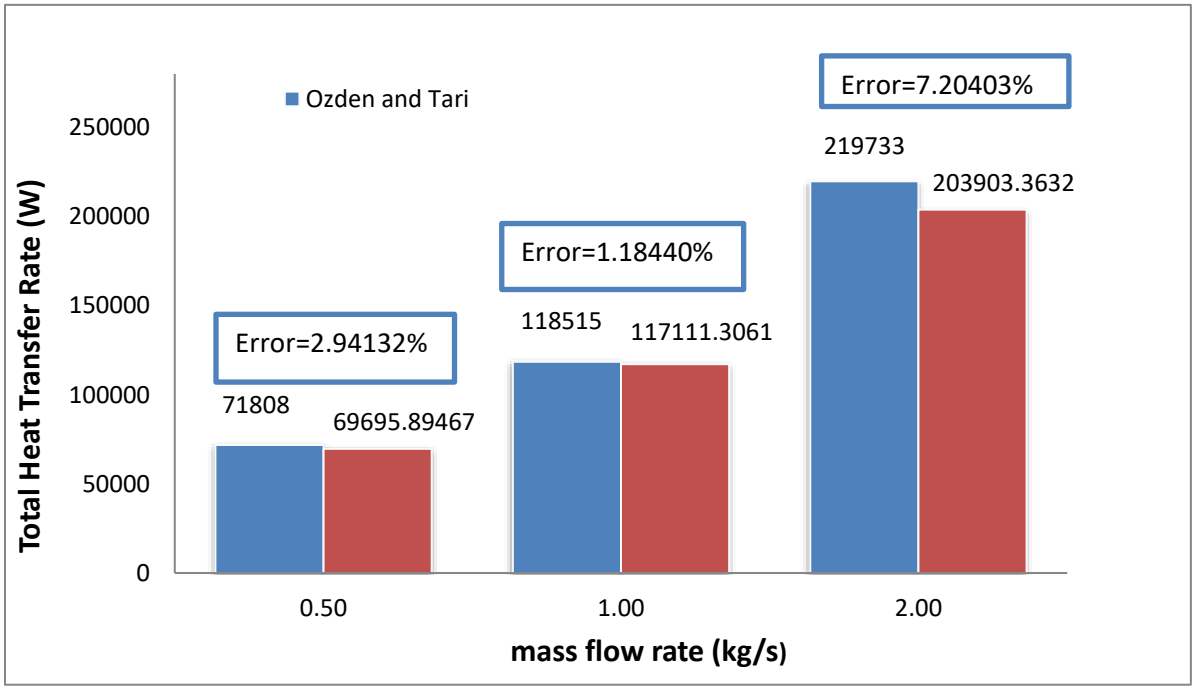
Error=7.20403%
219733
203903.3632
Ozden and Tari
250000
200000
150000
100000
50000
0
Total Heat Transfer Rate (W)
Error=1.18440%
118515
117111.3061
Error=2.94132%
71808
69695.89467
0.50
1.00
2.00
mass flow rate (kg/s)

(c)

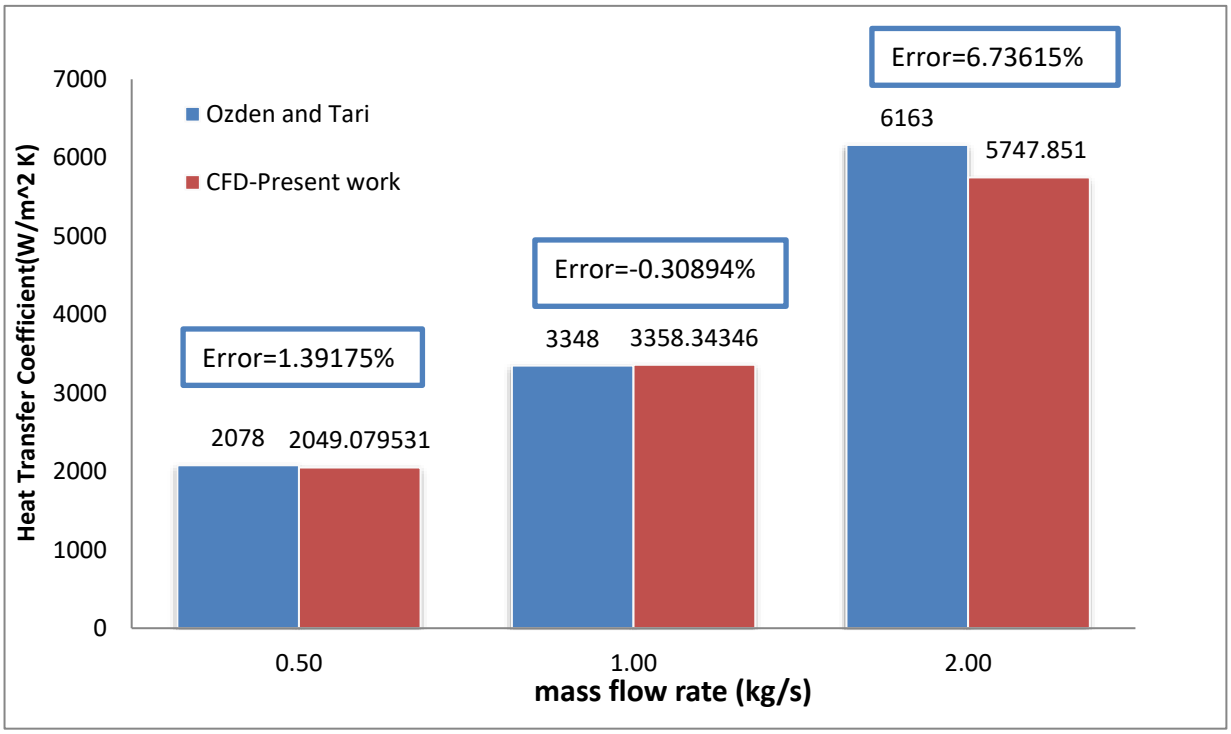

(d)

Fig. 5. Validation of the present CFD model against Ozden and Tari [35] for water at different shell-side mass flow rates: (a) shell-side outlet temperature, (b) shell-side pressure drop, (c) total heat-transfer rate and (d) heat-transfer coefficient.

3. Results and discussion

In this section, the numerical results are presented to assess the thermal–hydraulic performance of the baffled shell-and-tube heat exchanger with water as a base fluid with single nanofluids and hybrid nanofluids. The single nanofluids investigated include Al_2O_3/water, ZnO/water and GNP/water nanofluids and the hybrid nanofluids are Al_2O_3–ZnO/water, Al2O3–GNP/water and ZnO–GNP/water nanofluids. Shell-side outlet temperature, pressure drop, rate of heat transfer, average heat transfer coefficient and average Nusselt number are used to analyze the effect of Reynolds number, nanoparticle volume fraction and mass flow rate.

3.1 Effect of Reynolds number on the performance of single nanofluids

For water based single nanofluids, the influence of Reynolds number on the performance of the nanofluid was examined at a particular nanoparticle volume concentration of 5%. The inlet temperature to the shell was kept constant at 300 K, and the Reynolds number was varied between 10000 and 25000. The heat transfer results are presented in Fig. 6 for different outlet temperatures, pressure drop, heat transfer rate, average heat transfer coefficient and average Nusselt number of the shell side.

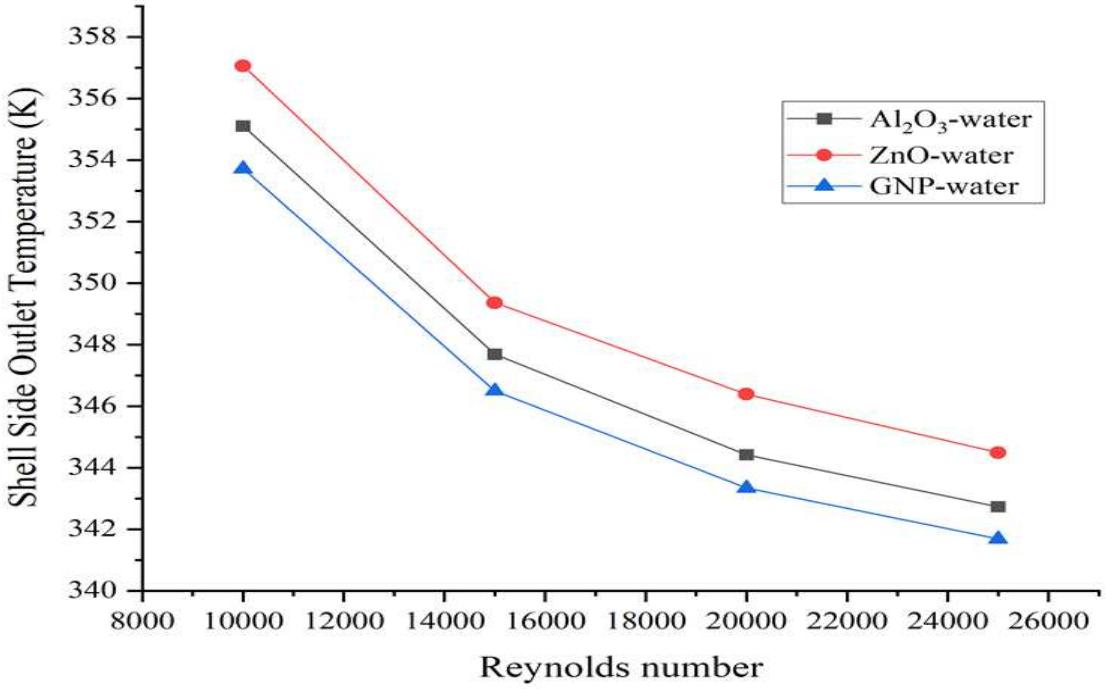

(a)

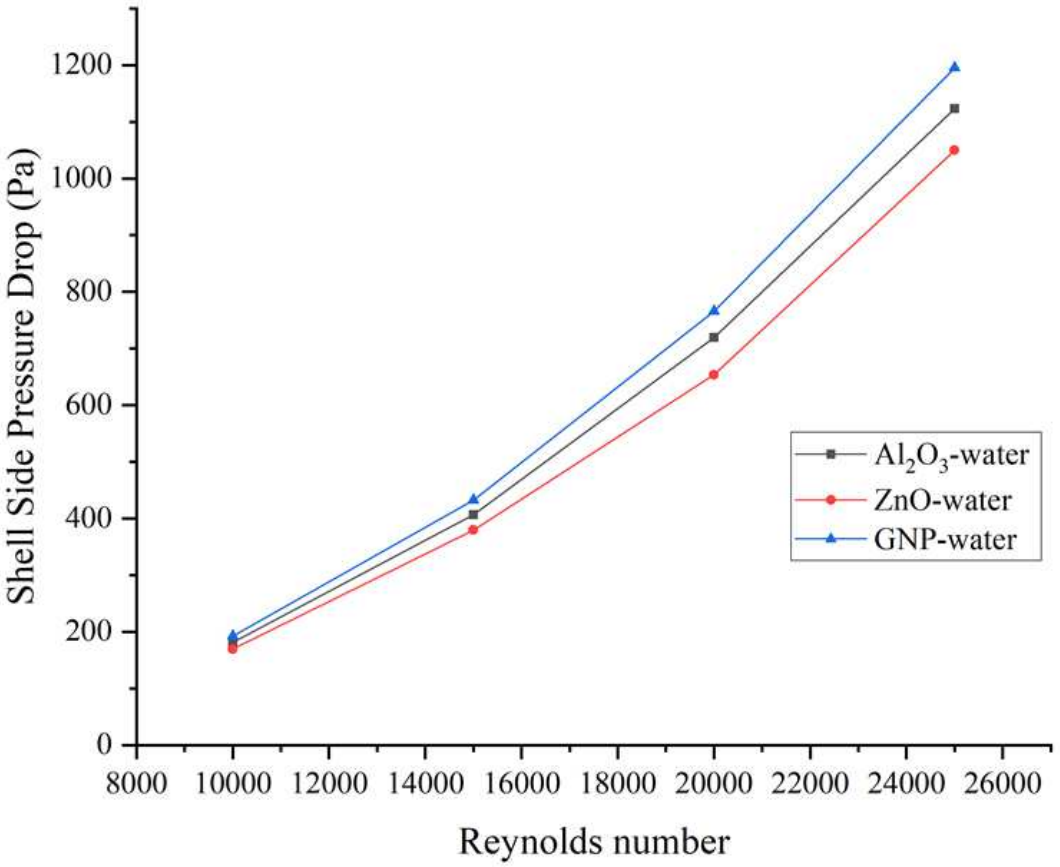
Shell Side Pressure Drop (Pa)
1200
1000
800
600
400
200
0
8000
10000
12000
14000
16000
18000
20000
22000
24000
26000
Reynolds number
Al2O3-water
ZnO-water
GNP-water

(b)

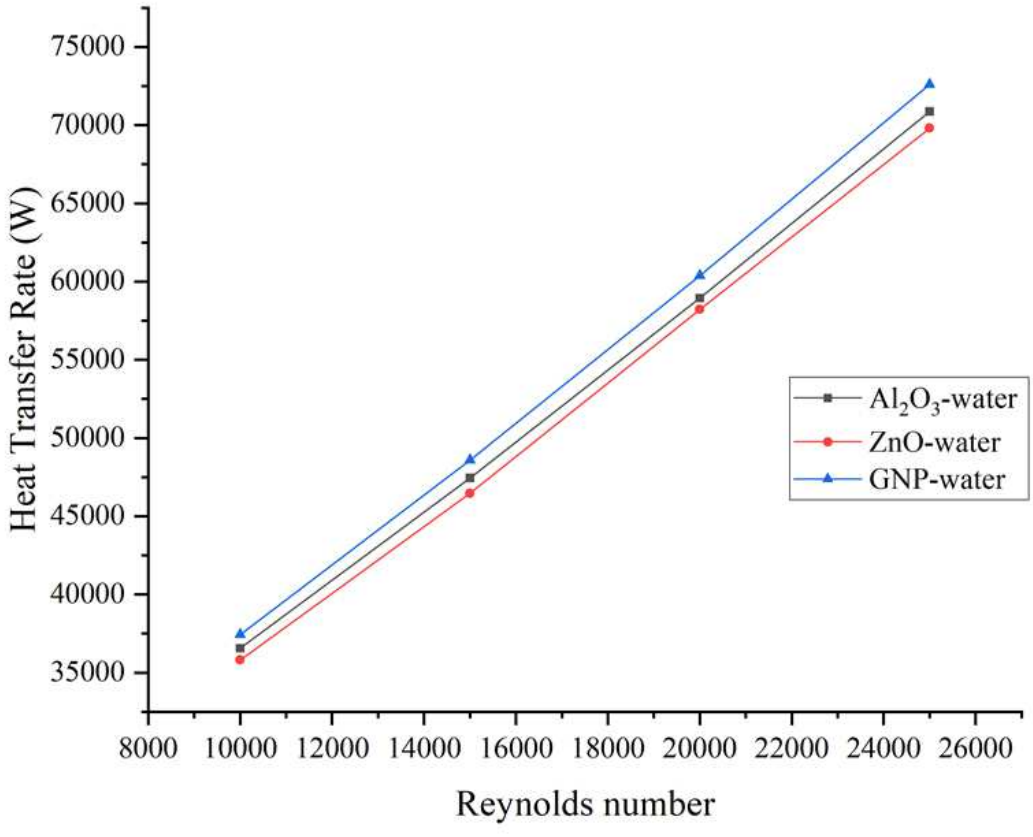
Heat Transfer Rate (W)
75000
70000
65000
60000
55000
50000
45000
40000
35000
8000
10000
12000
14000
16000
18000
20000
22000
24000
26000
Reynolds number
Al2O3-water
ZnO-water
GNP-water

(c)

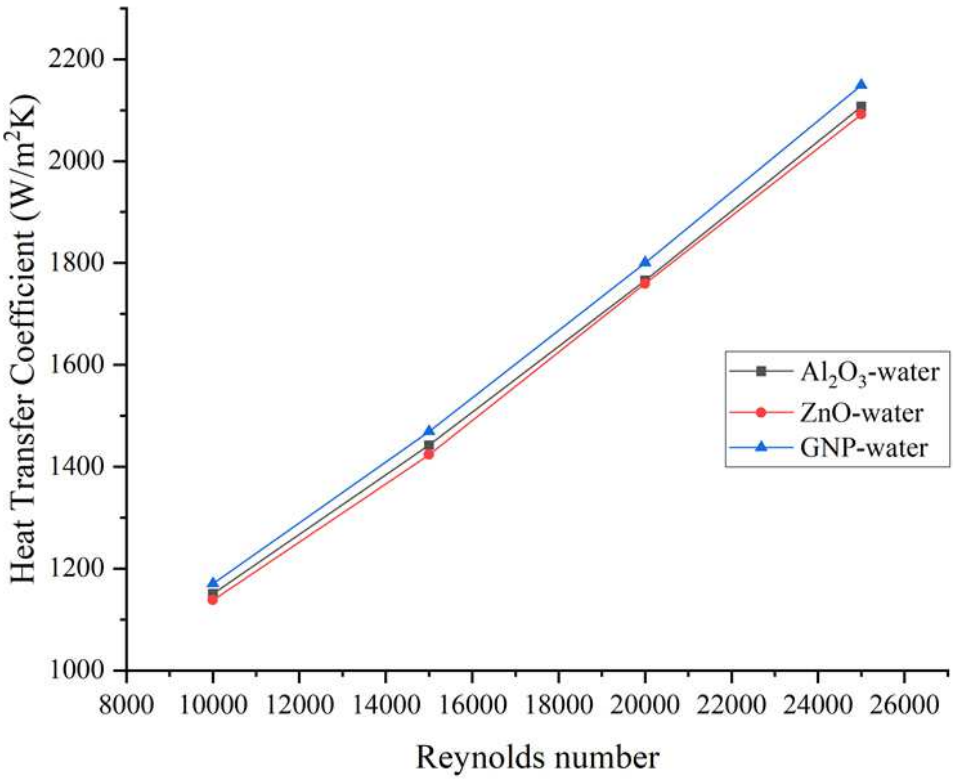
Heat Transfer Coefficient (W/m²K)
2200
2000
1800
1600
1400
1200
1000
8000
10000
12000
14000
16000
18000
20000
22000
24000
26000
Reynolds number
Al2O3-water
ZnO-water
GNP-water

(d)

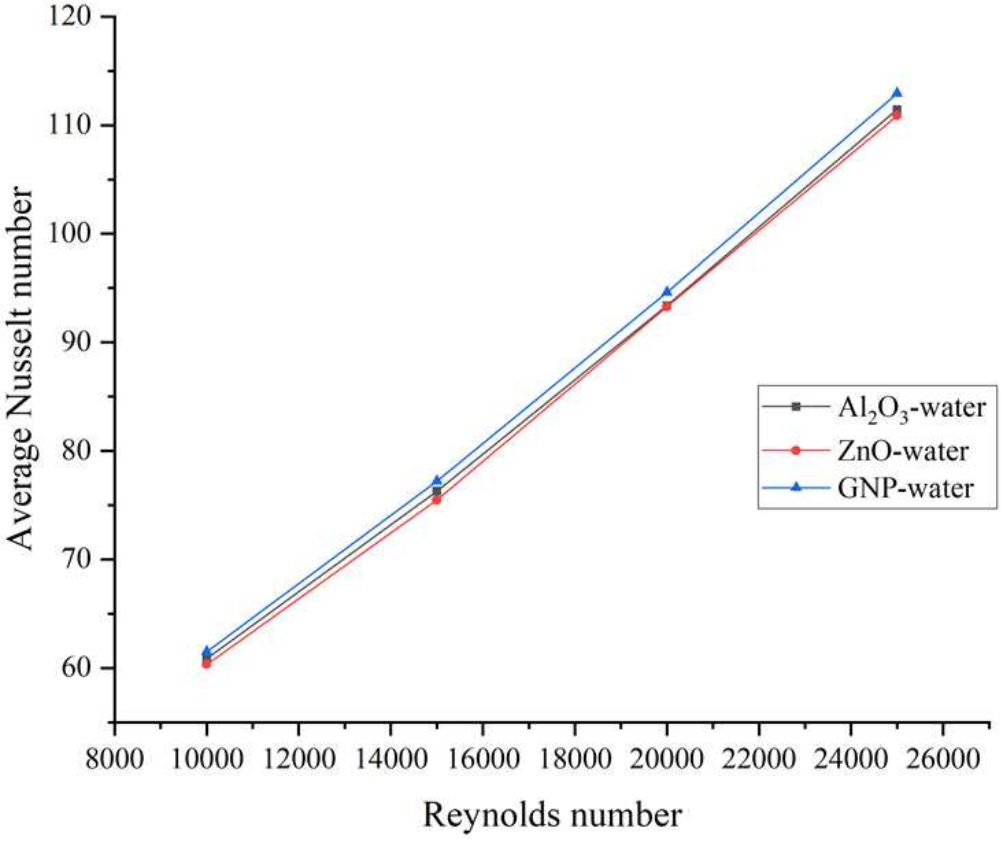
Average Nusselt number
120
110
100
90
80
70
60
8000
10000
12000
14000
16000
18000
20000
22000
24000
26000
Reynolds number
Al2O3-water
ZnO-water
GNP-water

(e)

Fig. 6. Effect of Reynolds number on the performance of single nanofluids at $\phi = 5\%$: (a) shell-side outlet temperature, (b) shell-side pressure drop, (c) heat transfer rate, (d) heat transfer coefficient, and (e) average Nusselt number

Fig. 6. Results for performance of single Nanofluids at ϕ=5% as a function of Reynolds number are presented as (a) shell-side outlet temperature, (b) shell-side pressure drop, (c) heat transfer rate, (d) average heat transfer coefficient and (e) average Nusselt number. Fig. 6(a) shows that for all single nanofluids, the shell-side outlet temperature drops off as the Reynolds number increases. The shell-side outlet temperature of ZnO/water is the highest in the range of Reynolds numbers investigated and that of GNP/water is the lowest one.The outlet temp of Al_2O_3/water falls between that of ZnO/water and GNP/water.As seen in figure 6(b), it can be seen that the shell-side pressure drop rises with increase in the Reynolds number for all the single nanofluids. Single nanofluids with GNP/water results in the highest pressure drop as compared to other nanofluids investigated in this study, while ZnO/water results in the lowest pressure drop. So, the higher the value of the Reynolds number, the better the flow intensity, but also the hydraulic resistance. From the results presented in figures 6(c) to (e), it is observed that for all single nanofluids, the rate of heat transfer, average heat transfer coefficient and average Nusselt number increase with the increase in Reynolds number. It is observed that GNP/water provides the highest value of heat transfer rate, heat transfer coefficient and average Nusselt number while the value of the same for ZnO/water is minimum. For these heat-transfer parameters, Al_2O_3/water is between GNP/water and ZnO/water. Thus, it is concluded that in single nanofluids, the GNP/water nanofluids have good performance in heat transfer with a high pressure drop.

3.2 Effect of nanoparticle volume fraction on the performance of single nanofluids

The performance of water-based single nanofluids with varying volume fraction of nanoparticles was investigated at a fixed Reynolds number of 10000. The volume fraction of the nanoparticles varied from 1% to 5%, and the inlet temperature of the shell side was fixed at 300K. The changes in the outlet temperature of the shell side, the pressure drop, the rate of heat transfer, the average heat transfer coefficient and the average Nusselt number are displayed in Fig. 7.

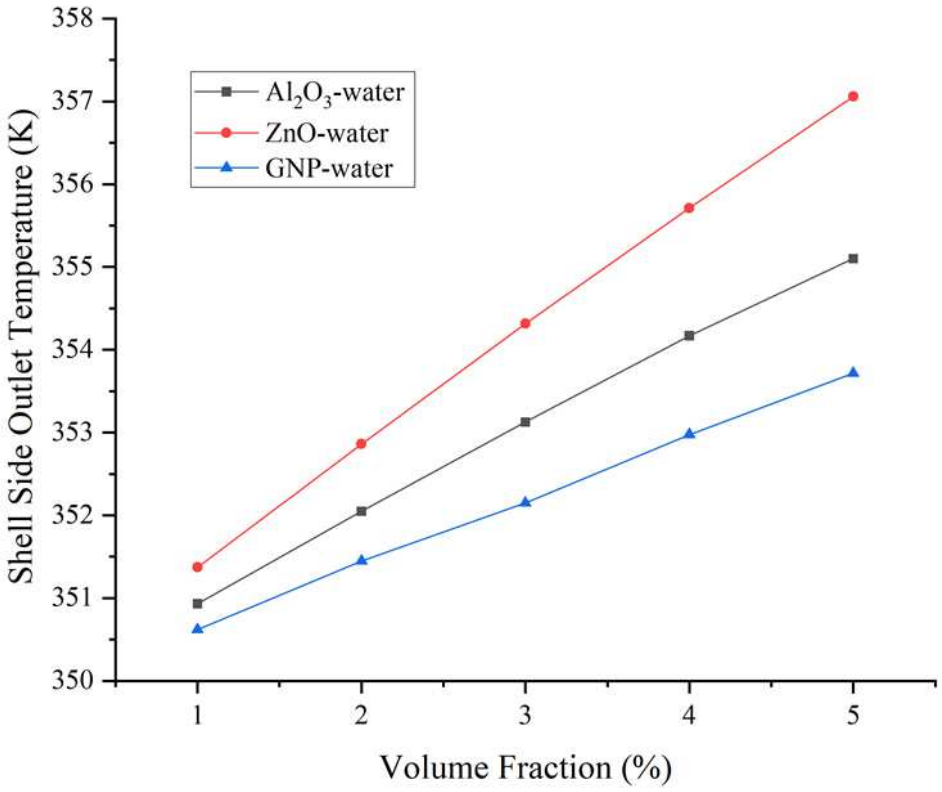
Shell Side Outlet Temperature (K)
Volume Fraction (%)
Al2O3-water
ZnO-water
GNP-water
358
357
356
355
354
353
352
351
350
1
2
3
4
5

(a)

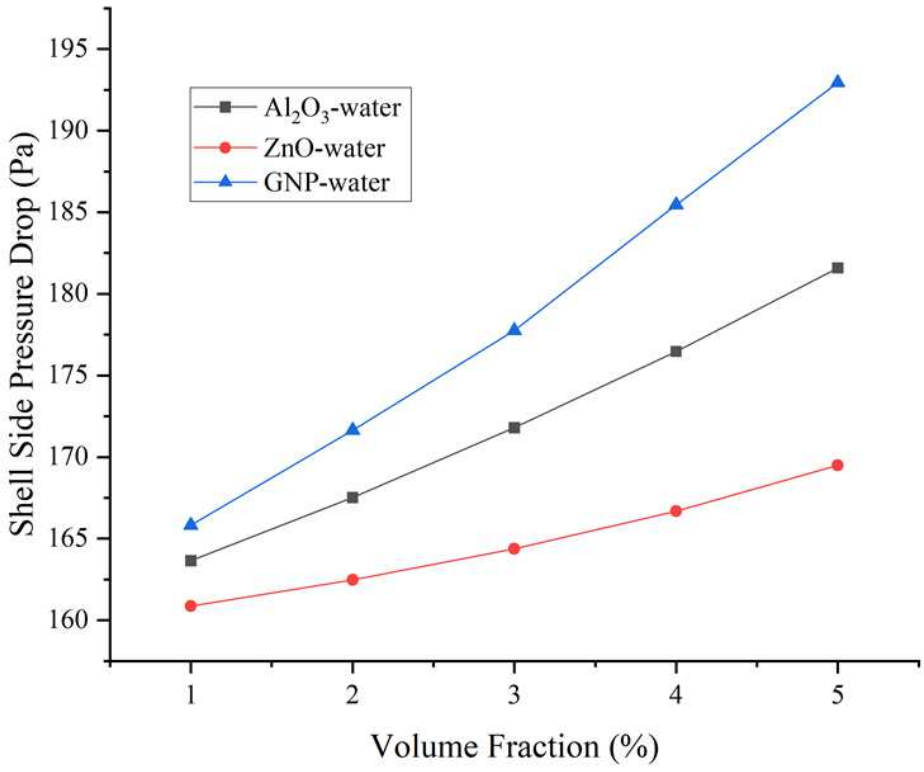
Shell Side Pressure Drop (Pa)
Volume Fraction (%)
Al2O3-water
ZnO-water
GNP-water
195
190
185
180
175
170
165
160
1
2
3
4
5

(b)

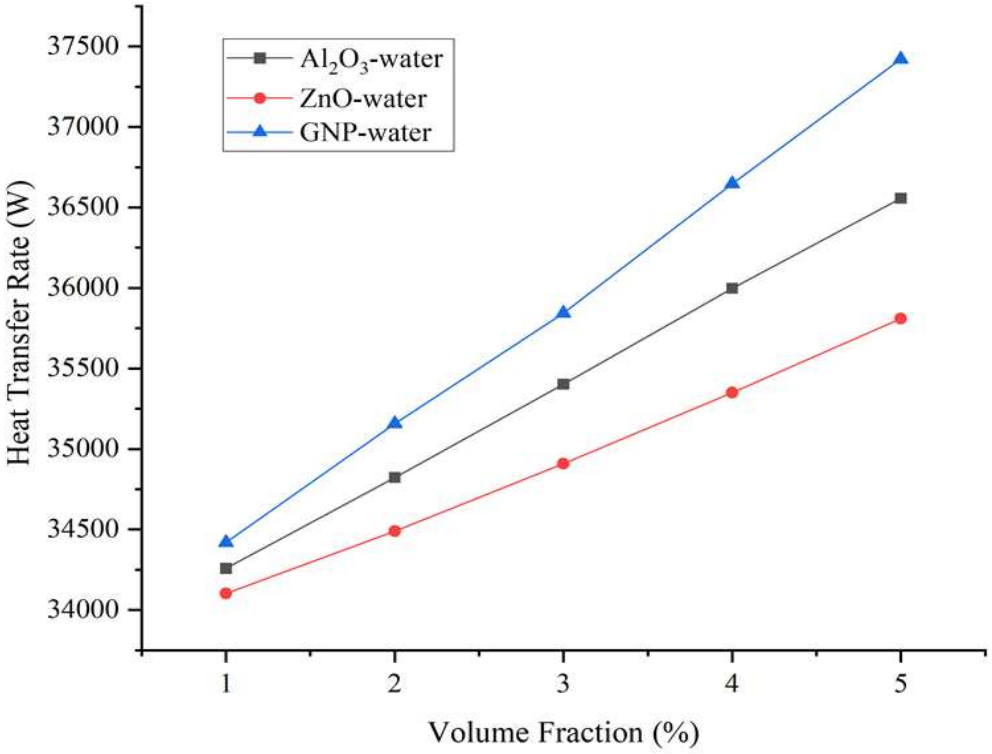
Heat Transfer Rate (W)
37500
37000
36500
36000
35500
35000
34500
34000
1
2
3
4
5
Volume Fraction (%)
Al2O3-water
ZnO-water
GNP-water

(c)

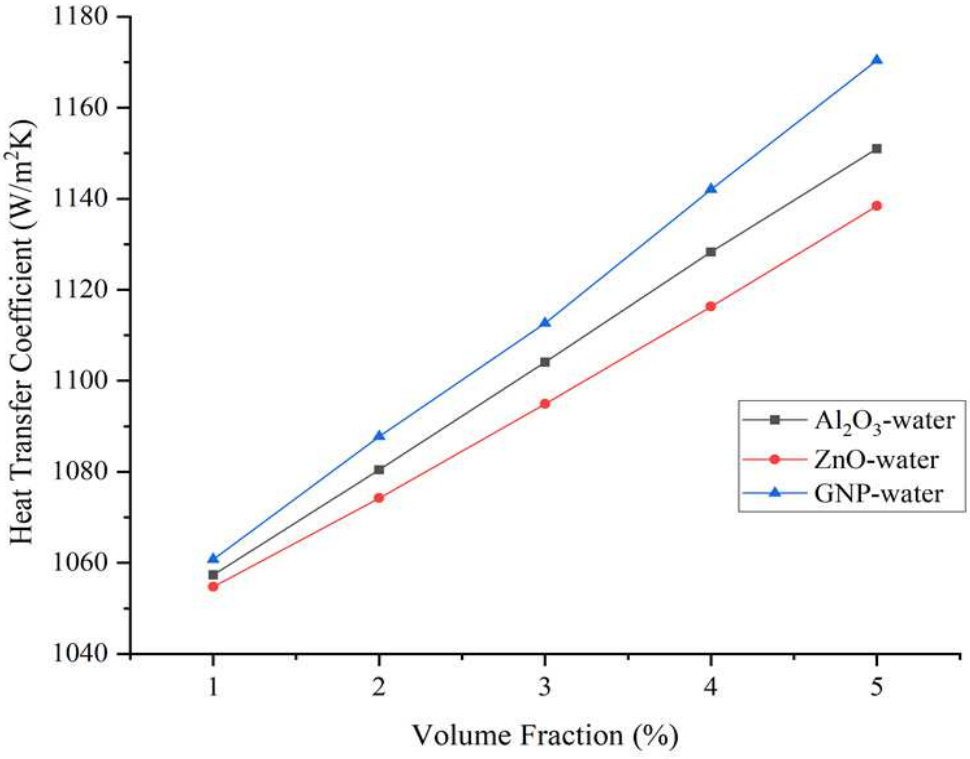
Heat Transfer Coefficient (W/m2K)
1180
1160
1140
1120
1100
1080
1060
1040
1
2
3
4
5
Volume Fraction (%)
Al2O3-water
ZnO-water
GNP-water

(d)

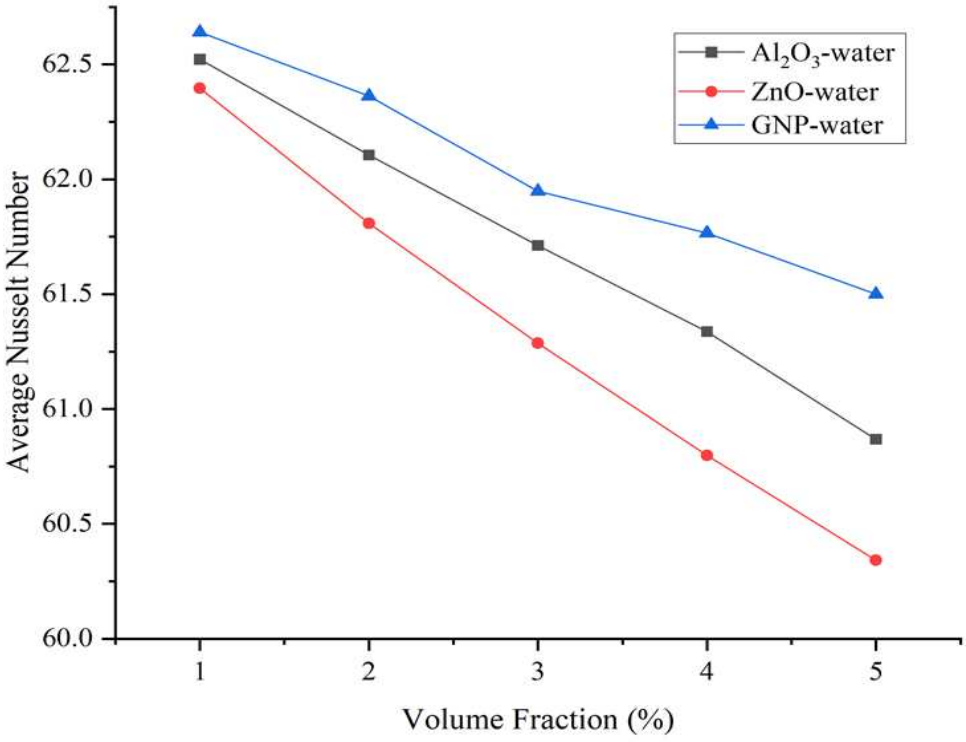

(e)

Fig. 7. Effect of nanoparticle volume fraction on the performance of single nanofluids at Re=10000 (a) shell-side outlet temperature, (b) shell-side pressure drop, (c) heat transfer rate, (d) heat transfer coefficient and (e) average Nusselt number.

It is observed from Fig. 7(a) that the outlet temperature of the shell side is increasing with nanoparticle volume fraction for all individual nanofluids. Among the mixtures, the highest outlet temperature is obtained for the ZnO/water mixture and the lowest outlet temperature is obtained from the GNP/water mixture for the entire concentration range. Al_2O_3/water is intermediate between ZnO/water and GNP/water.As can be seen in figure 7(b), the shell side pressure drop is found to be increasing with increasing nanoparticle volume fraction. For single nanofluids investigated, GNP/water results in the maximum pressure drop while the minimum pressure drop is obtained with ZnO/water. An intermediate pressure-drop response is observed for Al_2O_3/water. This means that the enhancement in the concentration of nanoparticles influences both the thermal and hydraulic characteristics of the shell-side flow.The results presented in figures 7(c) and 7(d) indicate that the heat transfer rate and the average heat transfer coefficient are increased as the

volume fraction of nanoparticles is increased. It can be concluded that GNP/water shows the highest rate of heat transfer and heat transfer coefficient, followed by Al_2O_3/water and ZnO/water. However, it is seen from Fig. 7(e) that the mean Nusselt number decreases for all the three nanofluids as the volume fraction increases, but GNP/water maintains the maximum Nusselt number and ZnO/water has the minimum value. Hence, for all the single nanofluids, GNP/water affords the highest heat-transfer performance and the highest pressure drop. The lowest pressure drop is observed for ZnO/water, and intermediate performance is obtained for Al_2O_3/water.

3.3 Effect of Reynolds number on the performance of hybrid nanofluids

The effect of Reynolds number on the performance of water-based hybrid nanofluids was performed for a fixed nanoparticle volume concentration of 5%. The hybrid nanofluids were prepared from two different nanoparticles of equal particle contribution. The Reynolds number was varied between 10000 and 25000. The effects of the changes of shell side outlet temperature, pressure drop, rate of heat transfer, average heat transfer coefficient, and average Nusselt number are presented as a function of position in Fig. 8(a) to (e).

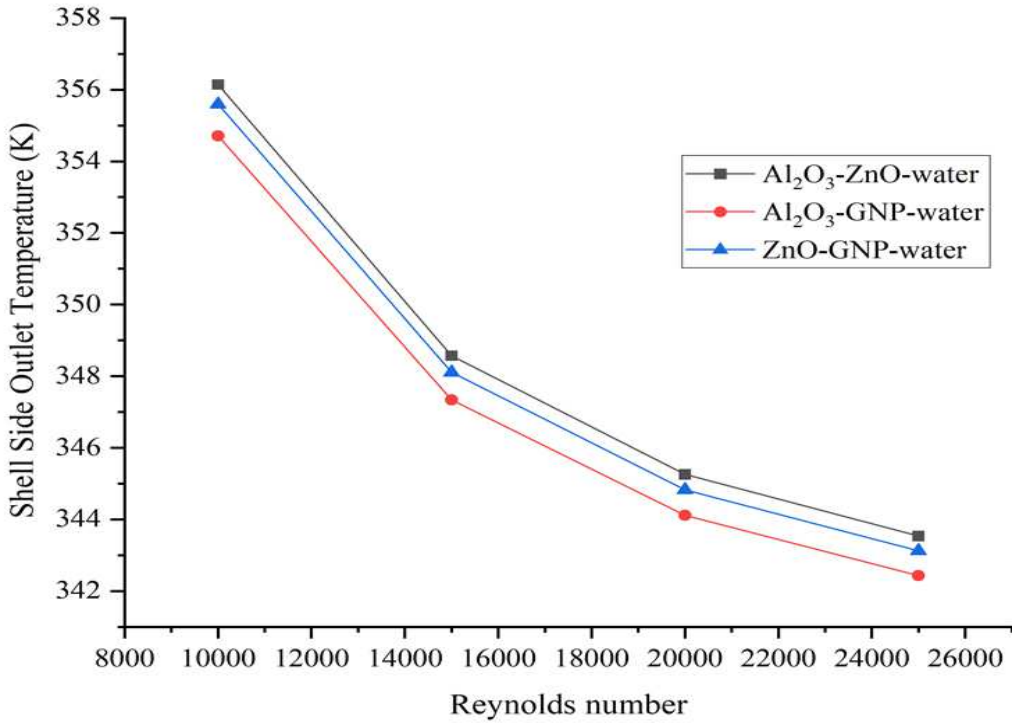

(a)

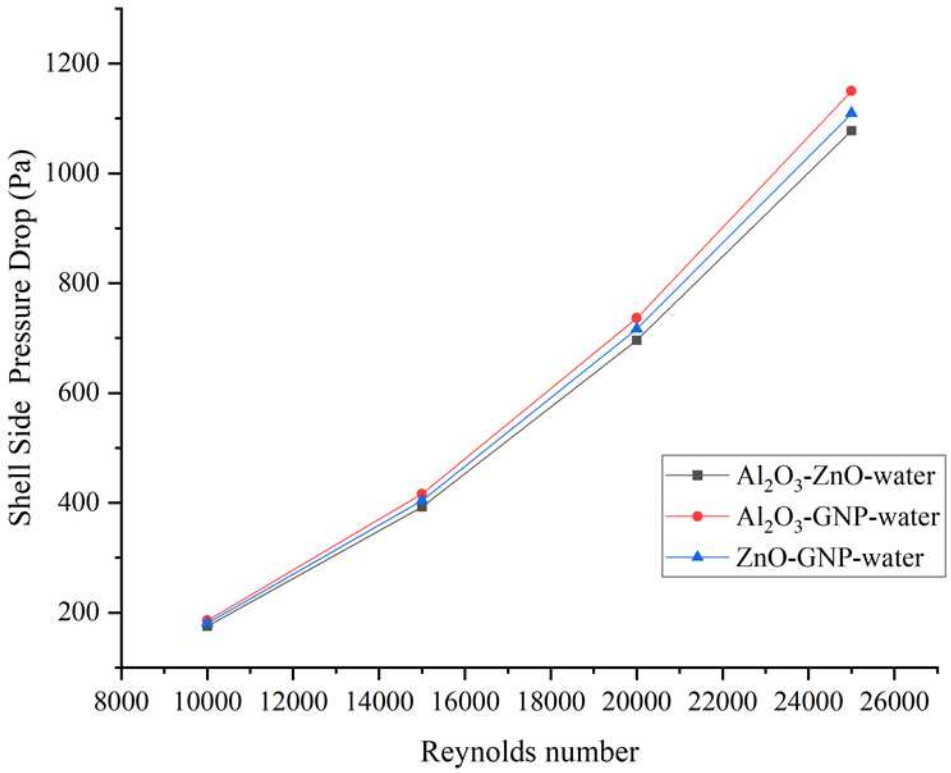
Shell Side Pressure Drop (Pa)
1200
1000
800
600
400
200
8000
10000
12000
14000
16000
18000
20000
22000
24000
26000
Reynolds number
Al2O3-ZnO-water
Al2O3-GNP-water
ZnO-GNP-water

(b)

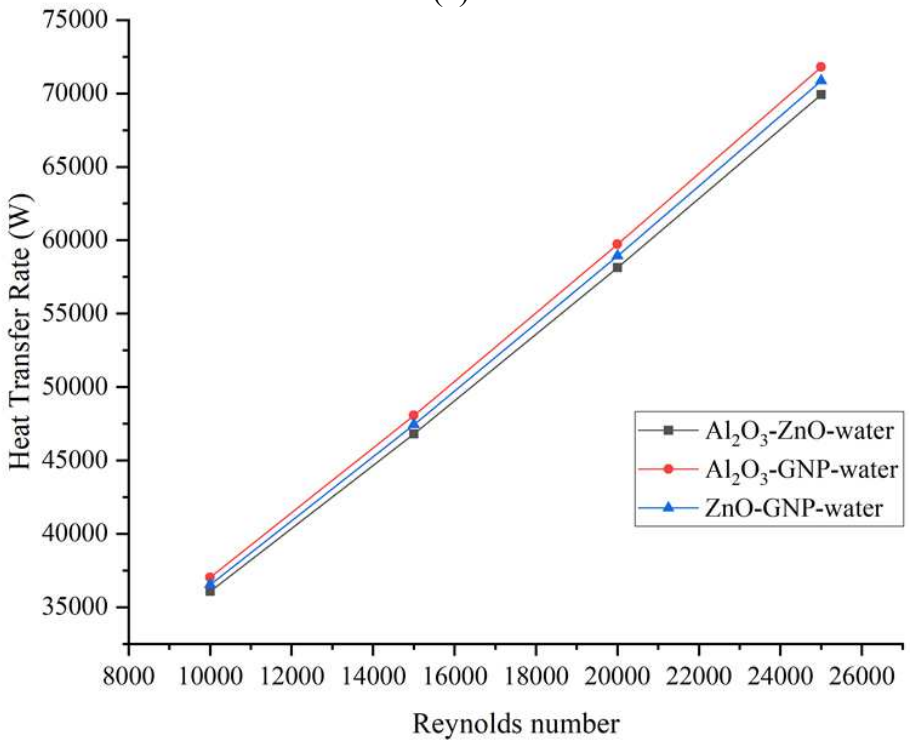
Heat Transfer Rate (W)
75000
70000
65000
60000
55000
50000
45000
40000
35000
8000
10000
12000
14000
16000
18000
20000
22000
24000
26000
Reynolds number
Al2O3-ZnO-water
Al2O3-GNP-water
ZnO-GNP-water

(c)

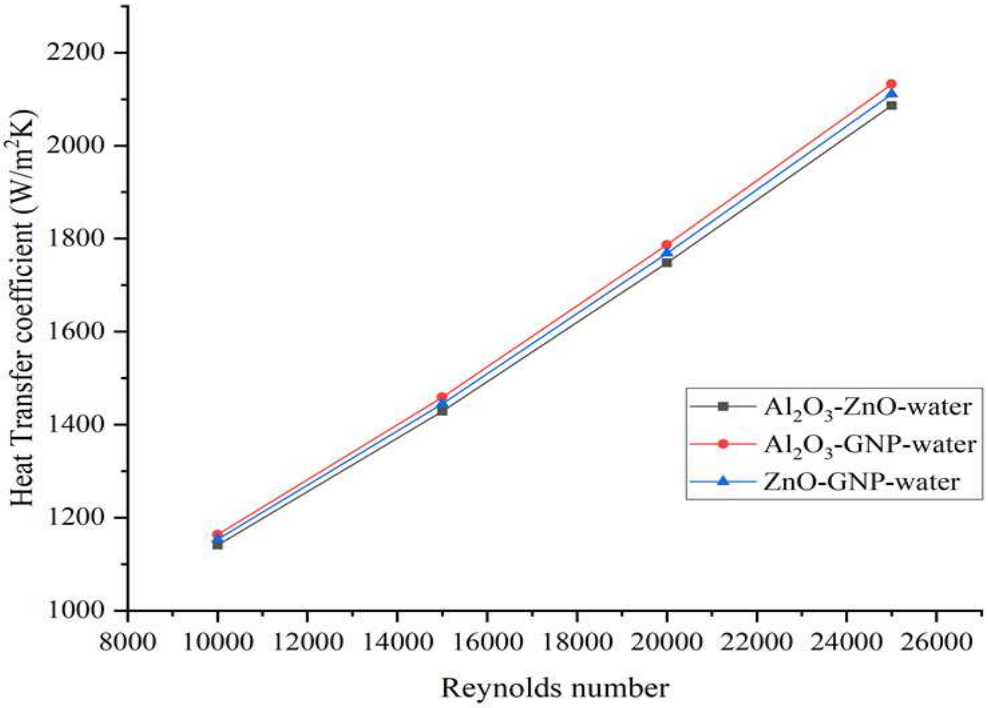
Heat Transfer coefficient (W/m²K)
2200
2000
1800
1600
1400
1200
1000
8000
10000
12000
14000
16000
18000
20000
22000
24000
26000
Reynolds number
Al2O3-ZnO-water
Al2O3-GNP-water
ZnO-GNP-water

(d)

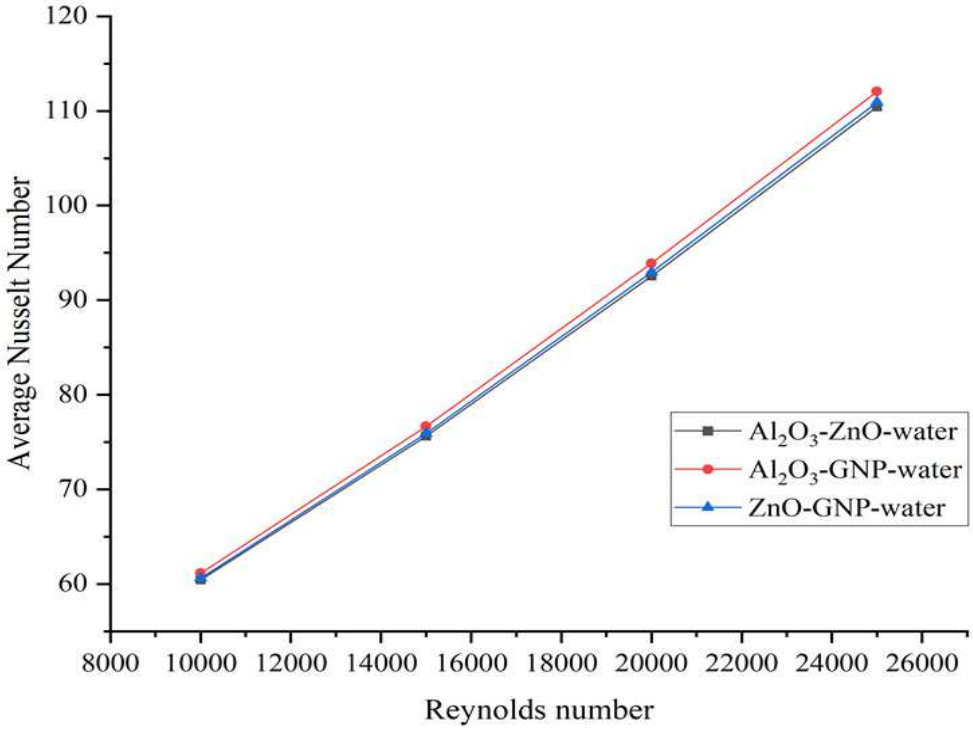
Average Nusselt Number
120
110
100
90
80
70
60
8000
10000
12000
14000
16000
18000
20000
22000
24000
26000
Reynolds number
Al2O3-ZnO-water
Al2O3-GNP-water
ZnO-GNP-water

(e)

Fig. 8. Effect of Reynolds number on the performance of hybrid nanofluids at ϕ=5%: (a) shell-side outlet temperature, (b) shell-side pressure drop, (c) heat transfer rate, (d) heat transfer coefficient, and (e) average Nusselt number.

It is seen from Fig. 8(a) that the outlet temperature of the shell side reduces as the Reynolds number increases for all hybrid nanofluids. Based on the results obtained in the present study, it is observed that the outlet temperature of Al_2O_3–ZnO/water is maximum among the hybrid nanofluids investigated followed by ZnO–GNP/water and Al_2O_3–GNP/water is found to have the lowest outlet temperature within the range of the investigated Reynolds numbers.It is seen in figure 8(b) that for all hybrid nanofluids, shell-side pressure drop is increasing with increasing Reynolds number. The Al_2O_3–GNP/water hybrid nanofluid has the highest pressure drop, while Al_2O_3–ZnO/water hybrid nanofluid has the lowest pressure drop among the hybrid nanofluids. This means that hydraulic resistance of the shell-side flow increases with increasing Reynolds number.It is observed from the results in Figures 8(c) to (e) that the rate of heat transfer, average heat transfer coefficient and average Nusselt number are all enhanced with the enhanced Reynolds number for all hybrid nanofluids. Al_2O_3–GNP/water has the highest heat transfer rate, heat transfer coefficient and average Nusselt number followed by ZnO–GNP/water. Al_2O_3–ZnO/water hybrid nanofluid exhibits the minimum values of these heat-transfer parameters compared with other hybrid nanofluids. So,Al_2O_3–GNP/water results in the best heat-transfer performance in this range of the Reynolds number, and it also leads to the greatest pressure drop.

3.4 Effect of nanoparticle volume fraction on the performance of hybrid nanofluids

The performance of water based hybrid nanofluids was analyzed for various nanoparticle volume fraction at a fixed Reynolds number of 10000. The nanoparticle volume fraction was varied from 1% to 5%. The variation of shell-side outlet temperature, pressure drop, heat transfer rate, average heat transfer coefficient and average Nusselt number are presented in Fig. 9(a) to (e).

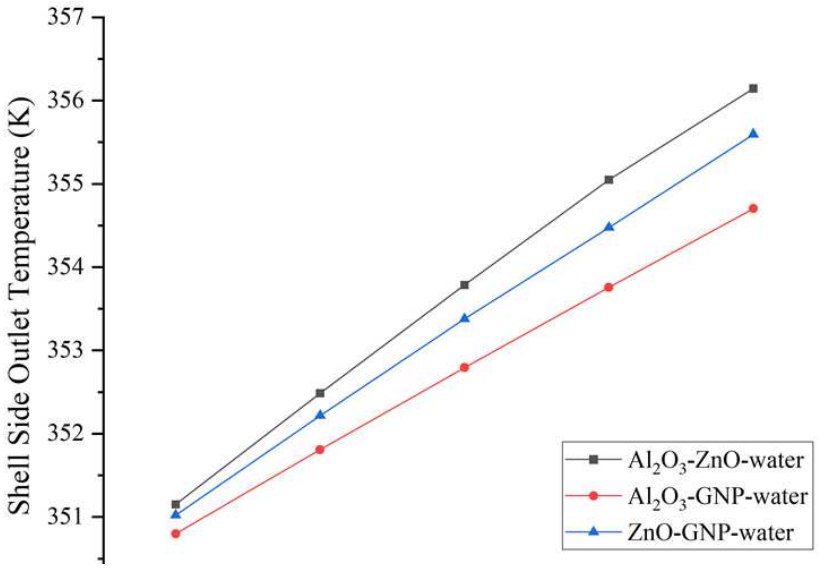
Shell Side Outlet Temperature (K)
357
356
355
354
353
352
351
Al2O3-ZnO-water
Al2O3-GNP-water
ZnO-GNP-water

(a)

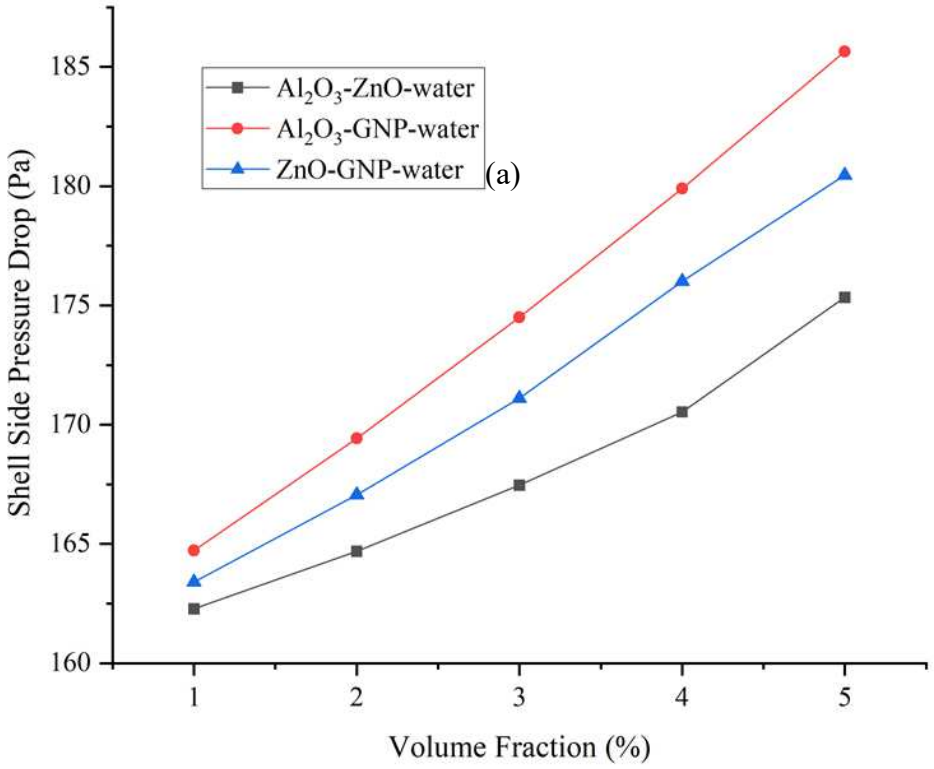
Shell Side Pressure Drop (Pa)
185
180
175
170
165
160
Al2O3-ZnO-water
Al2O3-GNP-water
ZnO-GNP-water
1
2
3
4
5
Volume Fraction (%)

(b)

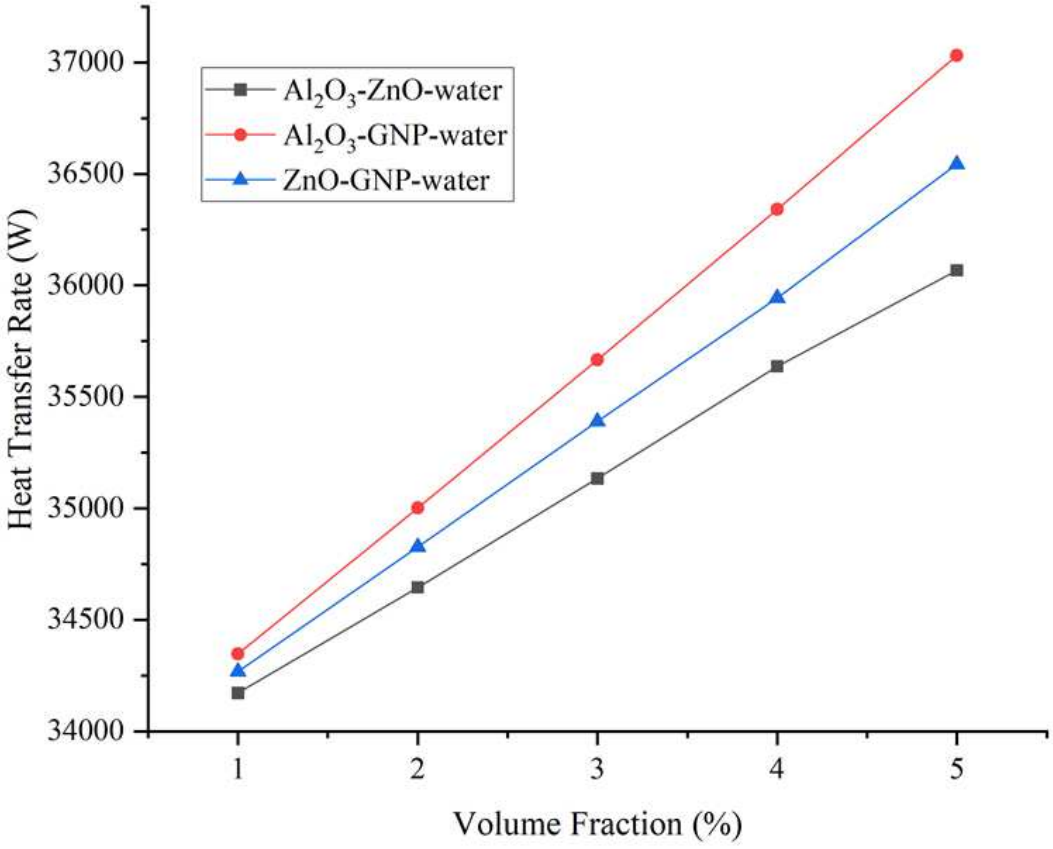
Heat Transfer Rate (W)
37000
36500
36000
35500
35000
34500
34000
1
2
3
4
5
Volume Fraction (%)
Al2O3-ZnO-water
Al2O3-GNP-water
ZnO-GNP-water

(c)

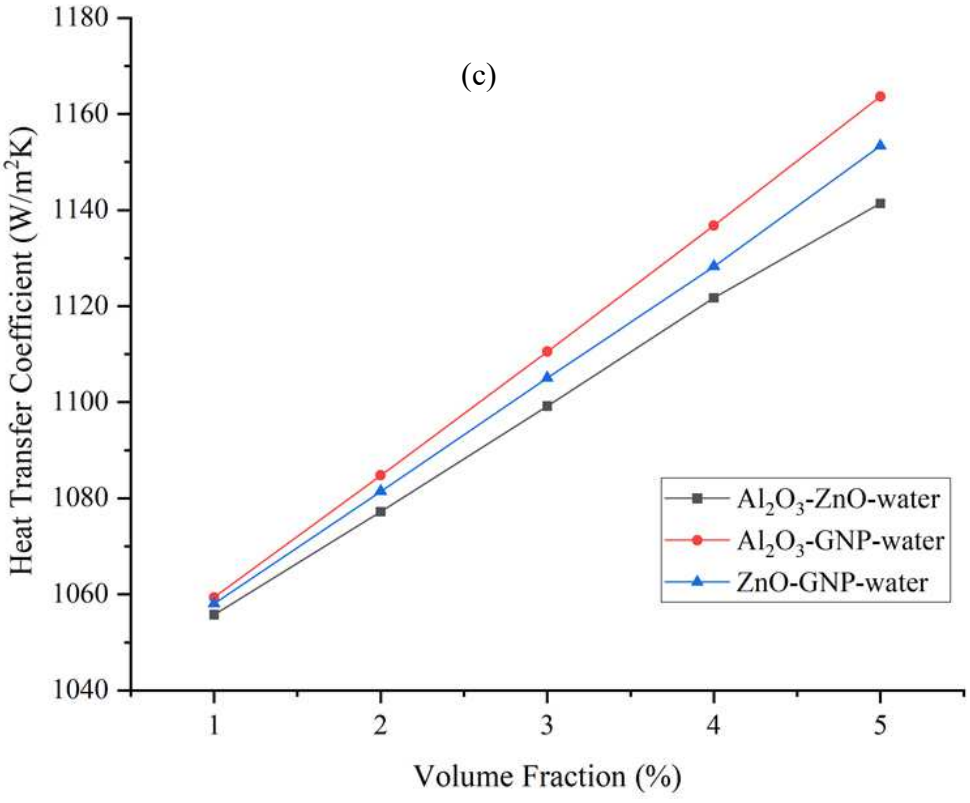
Heat Transfer Coefficient (W/m2K)
1180
1160
1140
1120
1100
1080
1060
1040
1
2
3
4
5
Volume Fraction (%)
Al2O3-ZnO-water
Al2O3-GNP-water
ZnO-GNP-water

(d)

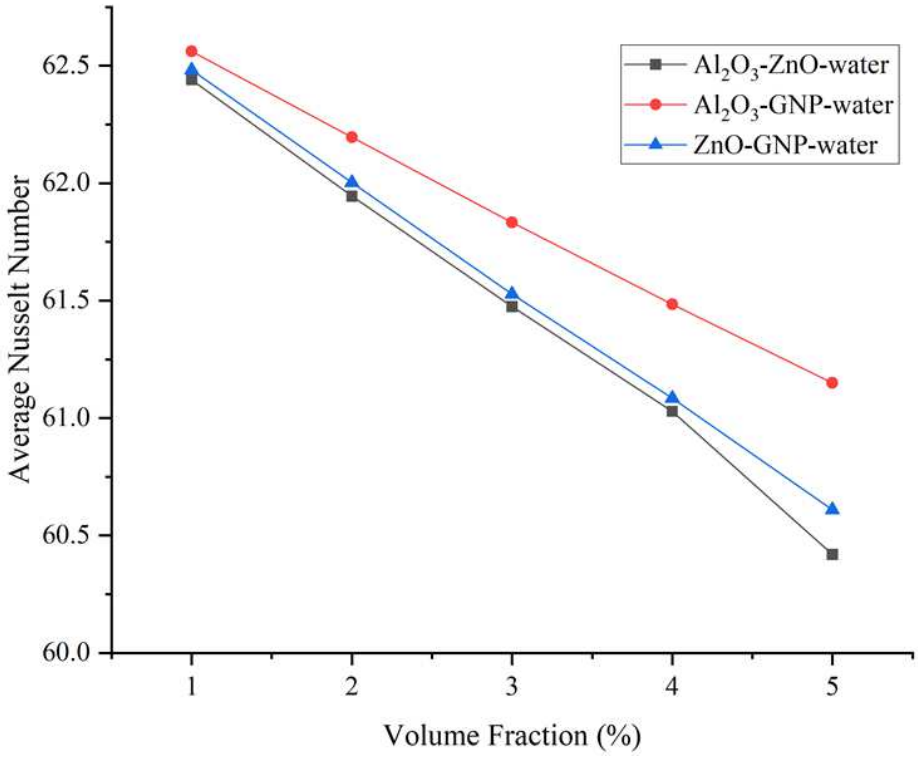

(e)

Fig. 9. Effect of nanoparticle volume fraction on the performance of hybrid nanofluids at Re=10000: (a) shell-side outlet temperature, (b) shell-side pressure drop, (c) heat transfer rate, (d) average heat transfer coefficient, and (e) average Nusselt number.

Fig. 9(a) indicates that the outlet temperature of the shell increases with increasing nanoparticle volume proportion of all hybrid nanofluids. The highest outlet temperature is obtained at all concentration levels for Al_2O_3–ZnO/water and the lowest outlet temperature is obtained for Al_2O_3–GNP/water. The behaviour of the ZnO–GNP/water is intermediate.As observed in Figure 9(b), the shell-side pressure drop is found to be increasing with an increase in the volume fraction of nanoparticles for all hybrid nanofluids. Among the various combinations, Al_2O_3–GNP/water combination exhibits the highest pressure drop and ZnO–GNP/water combination exhibits the second highest pressure drop while Al_2O_3–ZnO/water exhibits the lowest pressure drop. Hence, the higher the volume fraction of nanoparticles, the better is the thermal response, but higher is the

hydraulic resistance.Figures 9(c) and 9(d) reveal that the heat transfer rate and average heat transfer coefficient both rise with an increase of the nanoparticle volume fraction. The enhancements of the reported heat transfer rate are 9.49%, 8.29% and 7.07% for Al_2O_3–GNP/water, ZnO–GNP/water and Al_2O_3–ZnO/water, respectively, at ϕ=5% compared to pure water. These enhancements in the corresponding heat transfer coefficients are reported as 11.58%, 11.8% and 9.86% respectively. From these results, it can be said that the GNP containing hybrid nanofluids demonstrated superior heat-transfer properties as compared to Al_2O_3–ZnO/water under the investigated condition.Figure 9(e) shows that the average Nusselt number decreases with increasing volume fraction for all hybrid nanofluids. The maximum mean value of the Nu is obtained for ϕ=1%. The average enhancements of the Nusselt numbers are 4.16% for Al_2O_3–GNP/water, 4.04% for ZnO–GNP/water and 3.97% for Al_2O_3–ZnO/water at this concentration. Hence, the higher volume fraction leads to a better heat transfer rate and heat transfer coefficient while the present results indicate a decrease in the Nusselt number with higher particle loading.

3.5 Effect of mass flow rate on the performance of single nanofluids

The effect of shell-side mass flow rate on the performance of water-based single nanofluids was analysed at a fixed nanoparticle volume concentration of 5%. The mass flow rate was varied from 0.5 to 2.0 kg/s. The variations of shell-side outlet temperature, pressure drop and heat transfer rate are shown in Fig. 10(a) to (c).

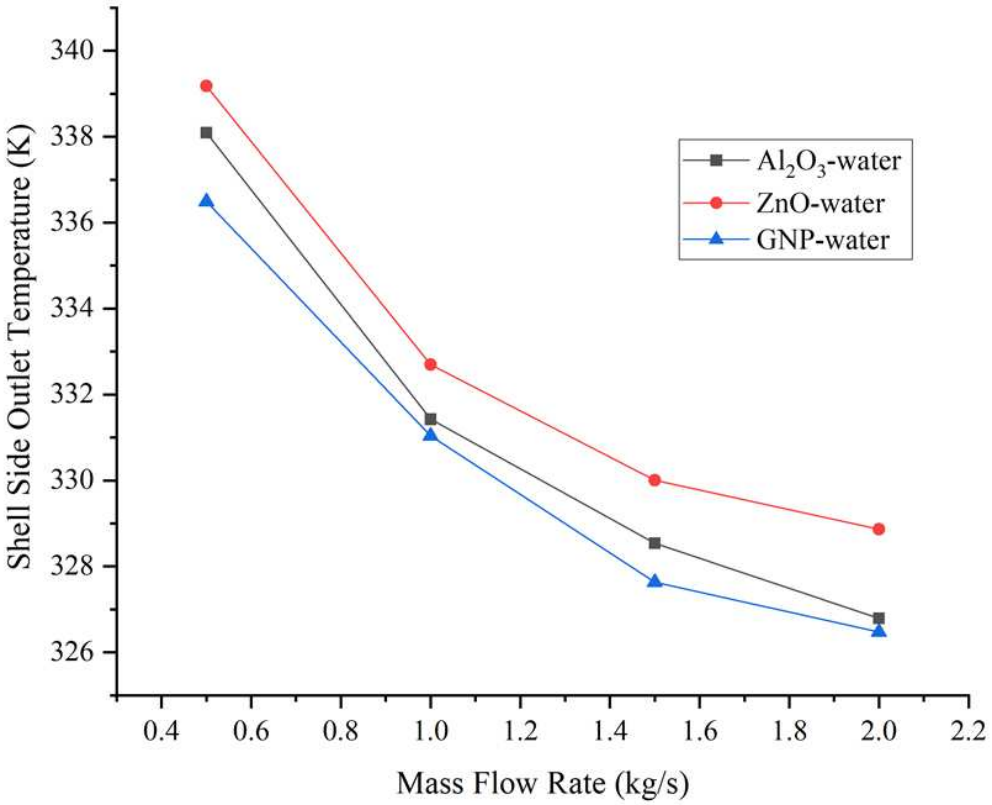
Shell Side Outlet Temperature (K)
340
338
336
334
332
330
328
326
0.4
0.6
0.8
1.0
1.2
1.4
1.6
1.8
2.0
2.2
Mass Flow Rate (kg/s)
Al2O3-water
ZnO-water
GNP-water

(a)

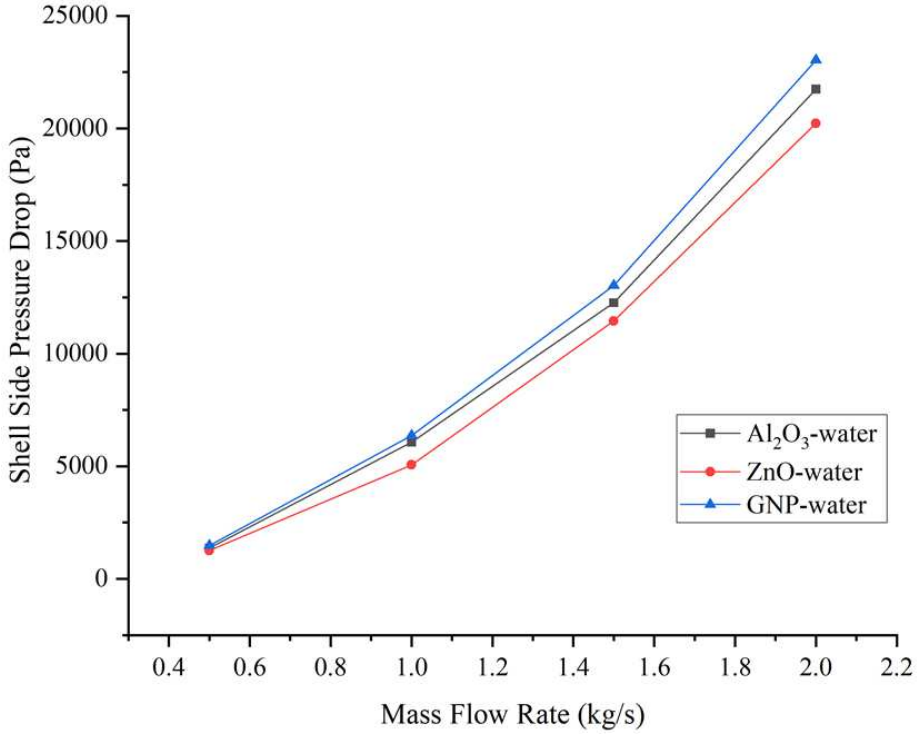
Shell Side Pressure Drop (Pa)
25000
20000
15000
10000
5000
0
0.4
0.6
0.8
1.0
1.2
1.4
1.6
1.8
2.0
2.2
Mass Flow Rate (kg/s)
Al2O3-water
ZnO-water
GNP-water

(b)

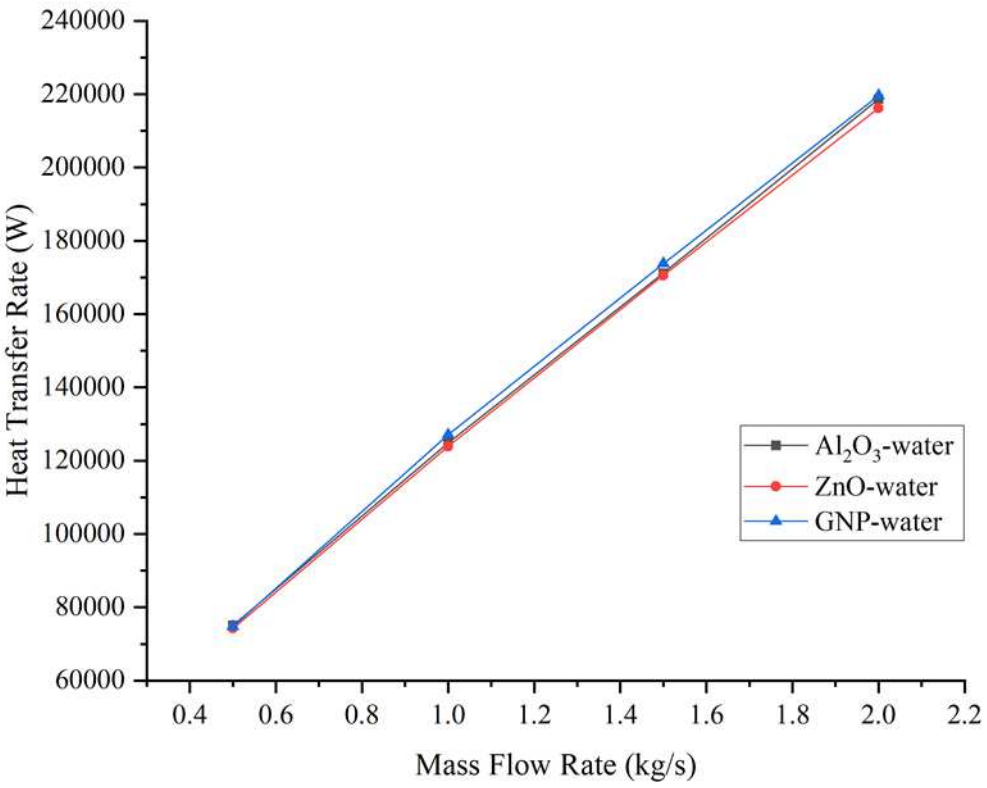

(c)

Fig. 10. Performance of single nanofluids at ϕ=5% with respect to mass flow rate for (a) shell-side outlet temperature, (b) shell-side pressure drop and (c) heat transfer rate.

From the outlet of the shell side as illustrated in Fig.10(a), it is seen that for all the single nanofluids the outlet temperature of the shell side decreases with increase in mass flow rate. ZnO/water provides the highest outlet temperature while GNP/water provides the lowest outlet temperature. ZnO/water exhibits approximately 1.72% higher outlet temperature than pure water at a mass flow rate of 0.5 kg/s.Figure 10(b) shows that the shell-side pressure drop increases with mass flow rate for all single nanofluids. But, the pressure drops of the nanofluids are less than that of pure water at the investigated mass-flow-rate condition. The pressure-drop decreases in comparison to pure water at 2.0 kg/s are 7.5%, 18.73% and 12.65% for GNP/water, ZnO/water and Al_2O_3/water respectively.In Figure 10(c), it can be seen that the heat transfer rate for all single nanofluids increases with the mass flow rate. It is found that GNP/water nanofluid provides the highest heat transfer rate among the single nanofluids investigated. At ϕ=5%, the heat transfer rate increases

by 9.17%, 7.18% and 6.13% for GNP/water, Al_2O_3/water and ZnO/water, respectively, compared with pure water. Hence, GNP/water can offer the greatest heat-transfer enhancement among the single nanofluids, while ZnO/water attains the lowest pressure-drop penalty.

3.6 Effect of mass flow rate on the performance of hybrid nanofluids

The performance of water-based hybrid nanofluids was studied at a constant volume concentration of ϕ=5% of nanoparticles and variable shell-side mass flow rate. The mass flow rate was varied between 0.5 kg /s to 2.0 kg /s. The variations of shell-side outlet temperature, pressure drop and heat transfer rate are shown in Fig. 11(a) to (c).

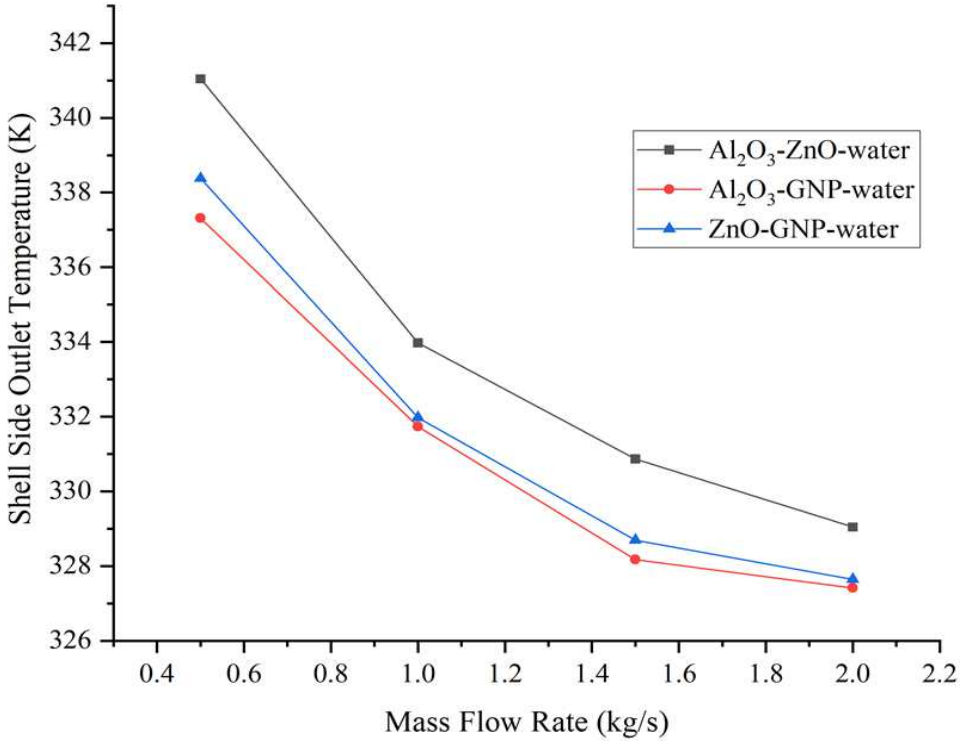

(a)

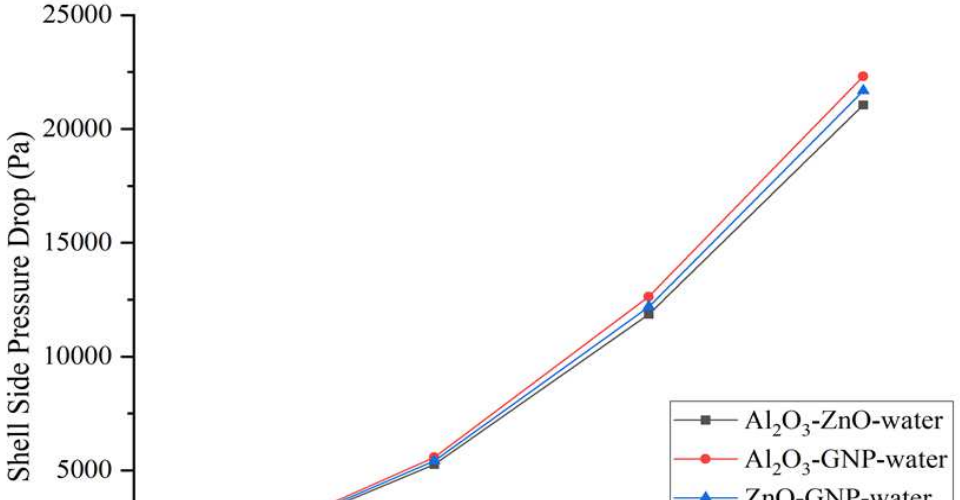

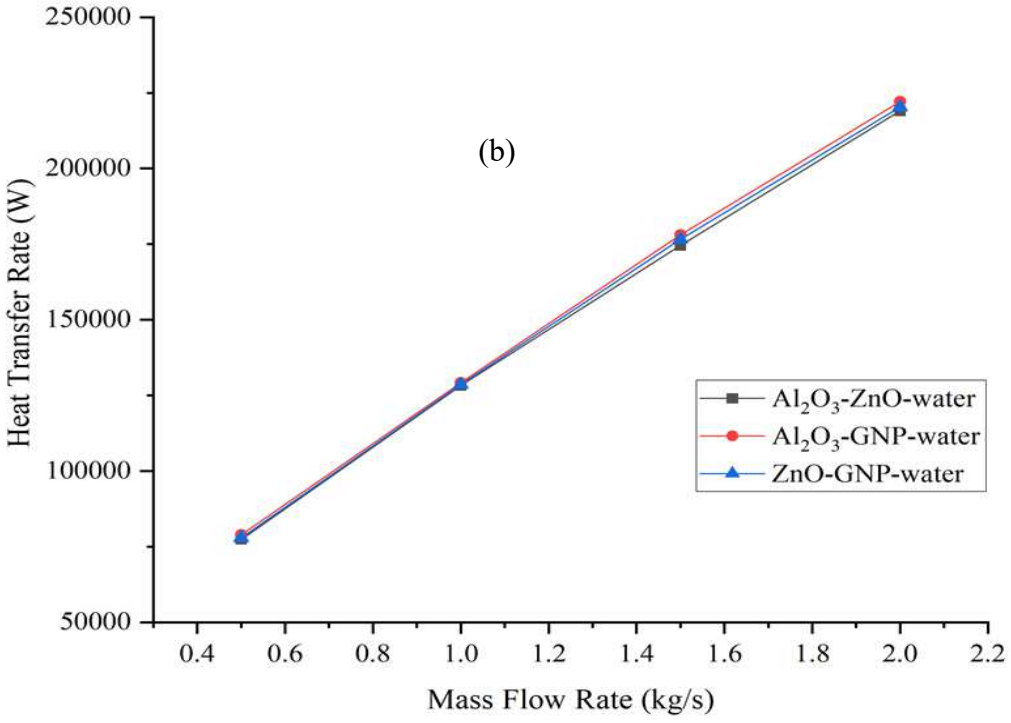

(c)

Fig. 11. Effect of mass flow rate on the performance of hybrid nanofluids at ϕ=5%: (a) shell-side outlet temperature, (b) shell-side pressure drop and (c) heat transfer rate.

From Fig. 11(a), it is seen that with increasing mass flow rate the shell-side outlet temperature decreases for all the hybrid nanofluids. It is observed that Al_2O_3 – ZnO/water hybrid nanofluids among the investigated hybrid nanofluids produces the highest outlet temperature followed by ZnO– GNP/water, Al_2O_3 – GNP/water produces the lowest outlet temperature.From figure 11(b) it is observed that the shell side pressure drop increases with increase in mass flow rate for all hybrid nanofluids.Al_2O_3–GNP/water has the highest pressure drop value while the lowest pressure

drop is obtained in Al_2O_3–ZnO/water hybrid nanofluids. It is found that the pressure drop of hybrid nanofluids is higher than the pure water in the considered operating condition. Figure 11(c) shows that the heat transfer rate increases with increasing mass flow rate. The heat transfer rate improves reported as 9.92%, 11.72% and 10.5% in Al_2O_3–ZnO/water, Al_2O_3–GNP/water and ZnO–GNP/water, respectively. So, it is obvious that the highest heat transfer rate is obtained with Al_2O_3–GNP/water and the highest pressure drop is also obtained.

3.7 Heat transfer rate enhancement analysis

The enhancement of the heat transfer rate of single nanofluids and hybrid nanofluids has been compared with pure water at Re=10000. The enhancement was studied at various volume fractions of nanoparticles as depicted in Fig. 12(a) and (b).

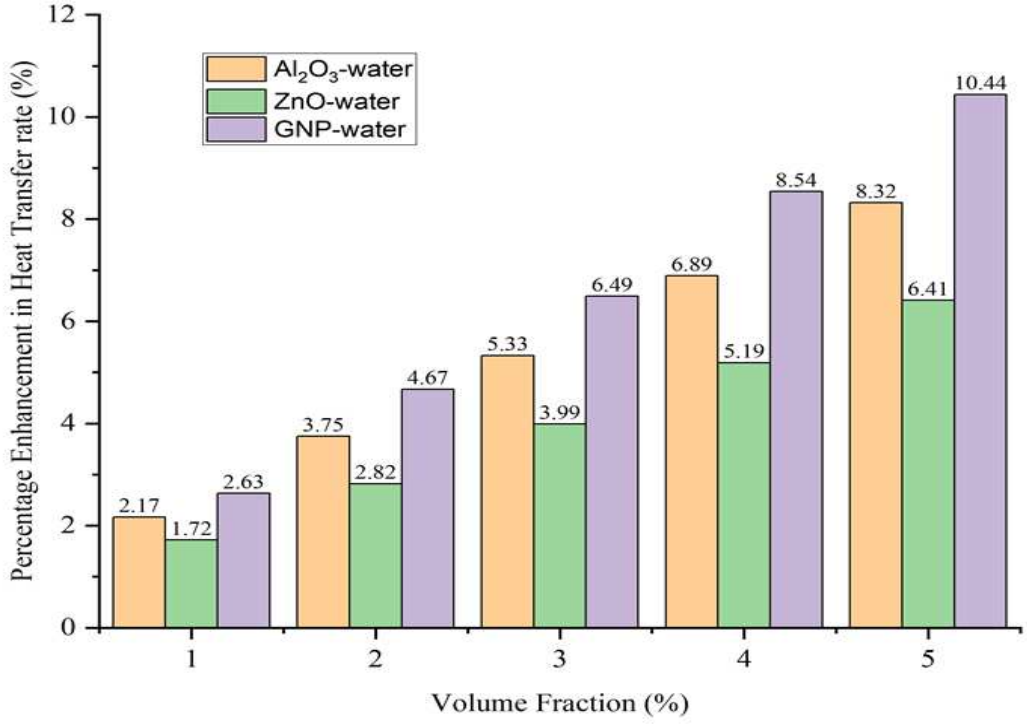

(a)

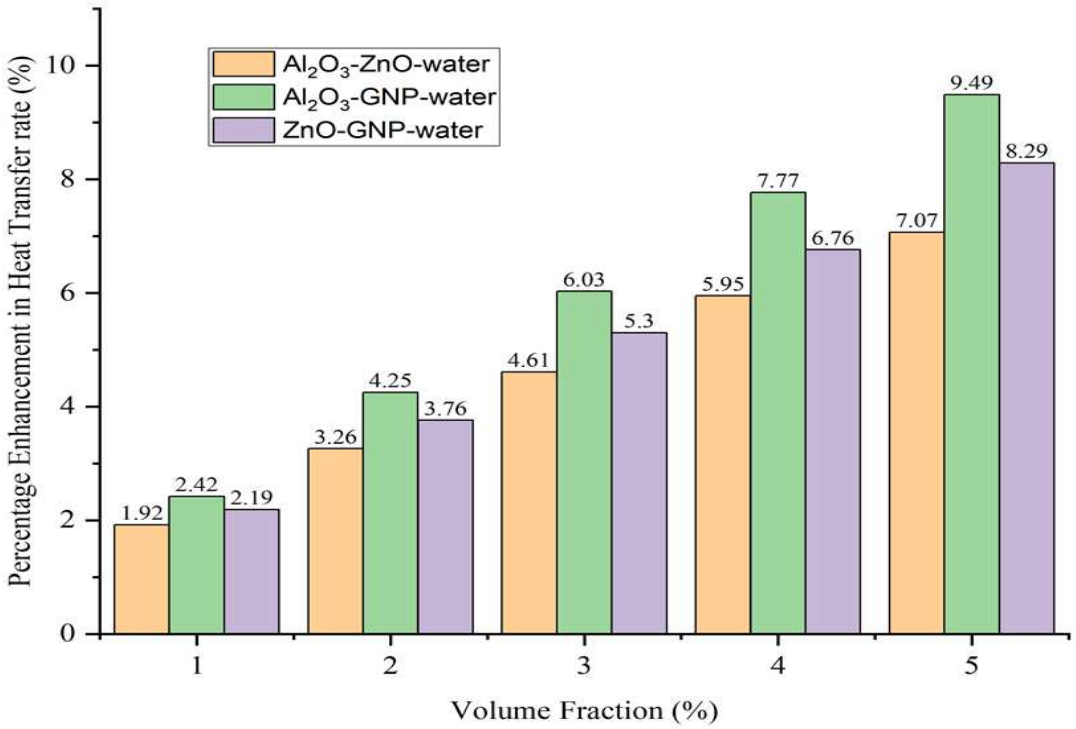

Fig. 12. Heat transfer rate enhancement relative to pure water at Re=10000: (a) single nanofluids (b) and (b) hybrid nanofluids.

From Fig. 12(a) it is seen that the enhancement of the heat transfer rate of single nanofluids is seen to increase with the volume fraction of the nanoparticles. GNP/water provides the most significant enhancement among the single nanofluids for the range of volume fractions investigated. GNP/water gives the maximum enhancement in heat transfer at ϕ=5% which is 10.44%. It is found that reinforcement of Al_2O_3/water is higher than that of ZnO/water and the least reinforcement is found in ZnO/water at ϕ=1% with reinforcement value as 1.72%.From Figure 12(b), it is seen that all hybrid nanofluids enhances the heat transfer rate than water. For all hybrid nanofluids, the enhancement is found to be increasing with nanoparticle volume fraction. Among them, Al_2O_3–GNP/water gives the highest enhancement over the investigated concentration range. The improvement in the heat transfer rate is 9.49% for Al_2O_3–GNP/water, 8.29% for ZnO–GNP/water, and 7.07% for Al_2O_3–ZnO/water at ϕ=5%. Thus, the results indicated that the heat transfer rate enhancement of nanofluids containing GNP and hybrid nanofluids are higher under the investigated condition.

3.8 Comparative analysis on the pressure, temperature and velocity fields

The quantitative results in the thermal–hydraulic analysis were complemented by the pressure, temperature and velocity fields analysis. The contour and flow-field results were reviewed for ϕ=5% and Re=10000. It is seen from Fig. 13 that the pressure contour for both single nanofluid and hybrid nanofluid.

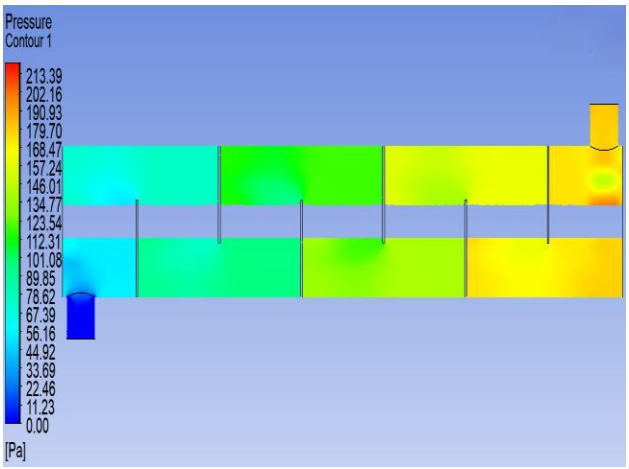

(a)

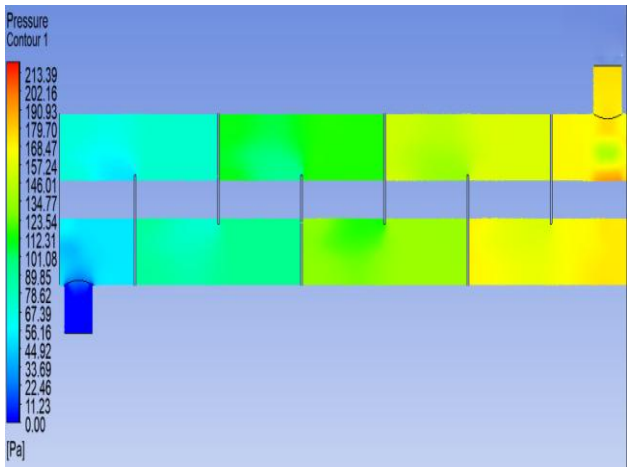

(d)

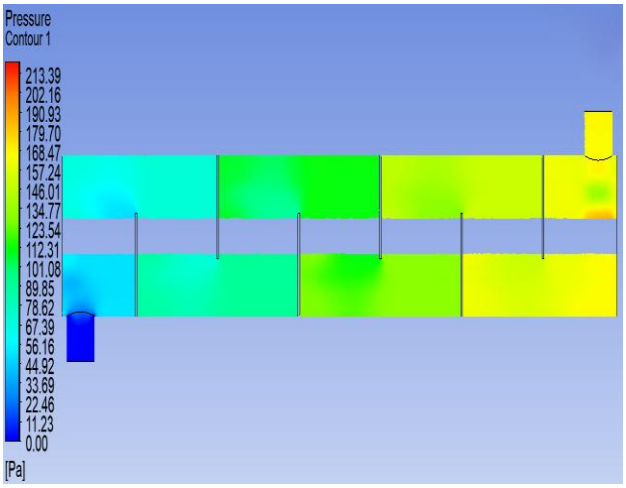

(b)

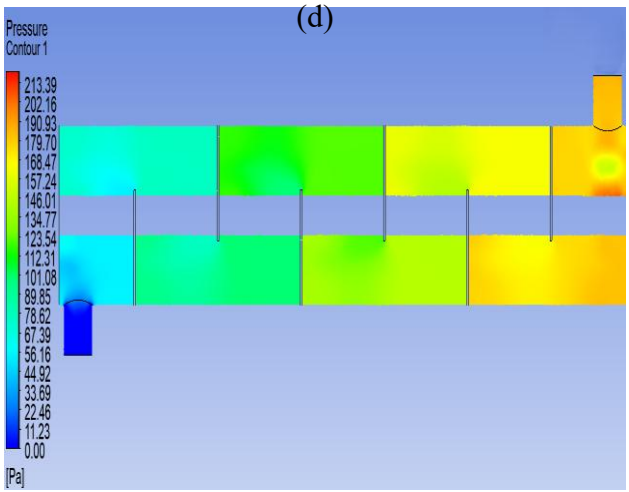

(e)

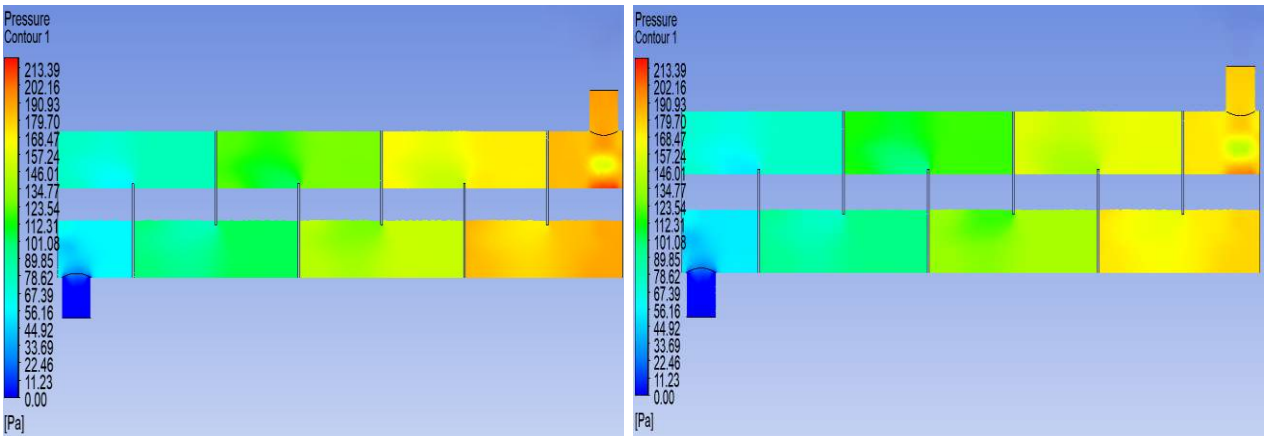

(c) (f)

Fig. 13. Pressure contours in the YZ plane at ϕ=5% and Re=10000: (a) Al_2O_3/water, (b) ZnO/water, (c) GNP/water, (d)Al_2O_3–ZnO/water, (e) Al_2O_3–GNP/water and (f) ZnO–GNP/water.

Pressure contours indicate that the pressure is reduced from shell-side inlet to the pressure outlet. The results indicate that the single nanofluids have the highest pressure loss for GNP/water and the lowest for ZnO/water. The hybrid nanofluids, Al_2O_3–GNP/water, experience the greatest pressure loss while Al_2O_3–ZnO/water experience the lowest pressure loss. These observations are in keeping with the trends in pressure drop discussed in previous sections.

The temperature contours for the investigated nanofluids and hybrid nanofluids are shown in Fig. 14.

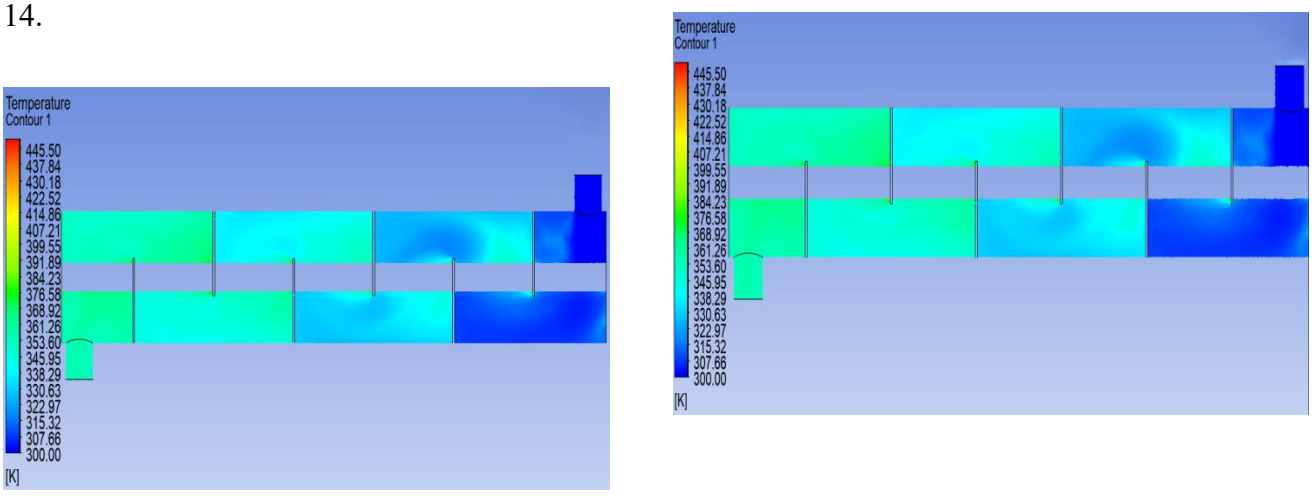

(a) (d)

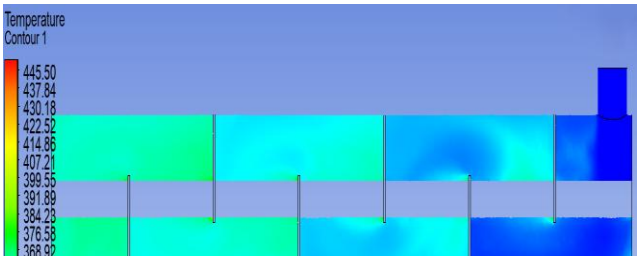

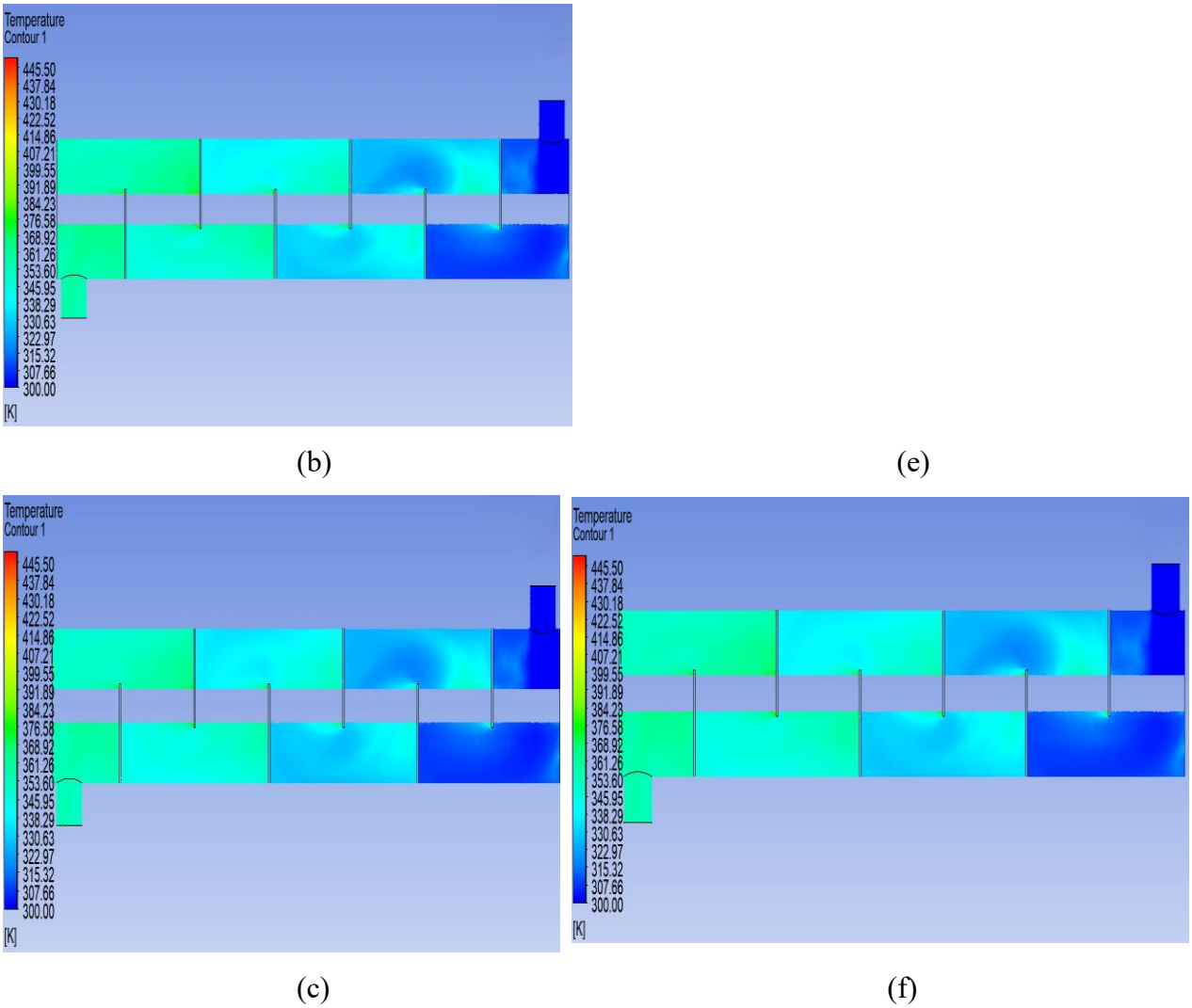

Fig. 14. Temperature contours in the YZ plane at ϕ=5% and Re=10000: (a) Al_2O_3/water, (b) ZnO/water, (c) GNP/water, (d) Al_2O_3–ZnO/water, (e)Al_2O_3–GNP/water and (f) ZnO–GNP/water.

The temperature contours indicate that the shell-side fluid temperature rises from the inlet region to the outlet region. It is observed that among the single nanofluids, the highest outlet-temperature distribution is obtained for ZnO/water nanofluid and the lowest outlet-temperature distribution is obtained for GNP/water nanofluid. It is observed that the outlet-temperature distribution of the hybrid nanofluids is highest for Al_2O_3–ZnO/water followed by ZnO–GNP/water and lowest for Al_2O_3–GNP/water.

The velocity field was also investigated for Al_2O_3/water with ϕ=5% and Re=10000 as depicted in Fig. 15.

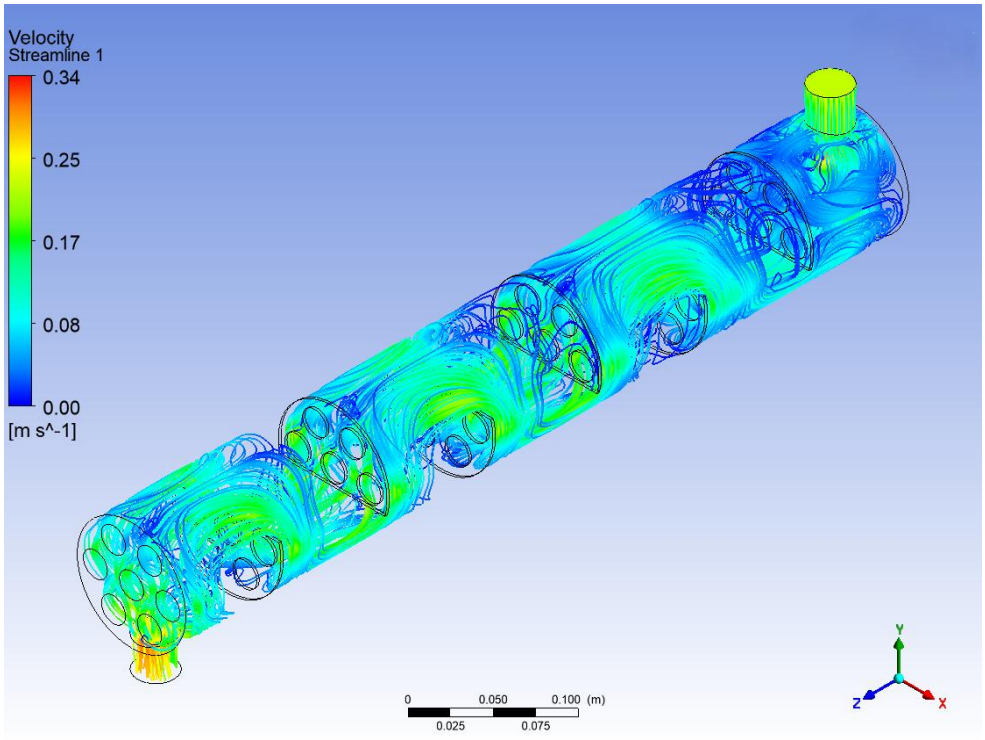
Velocity
Streamline 1
0.34
0.25
0.17
0.08
0.00
[m s^-1]
0
0.050
0.100 (m)
0.025
0.075
Y
Z
X

(a)

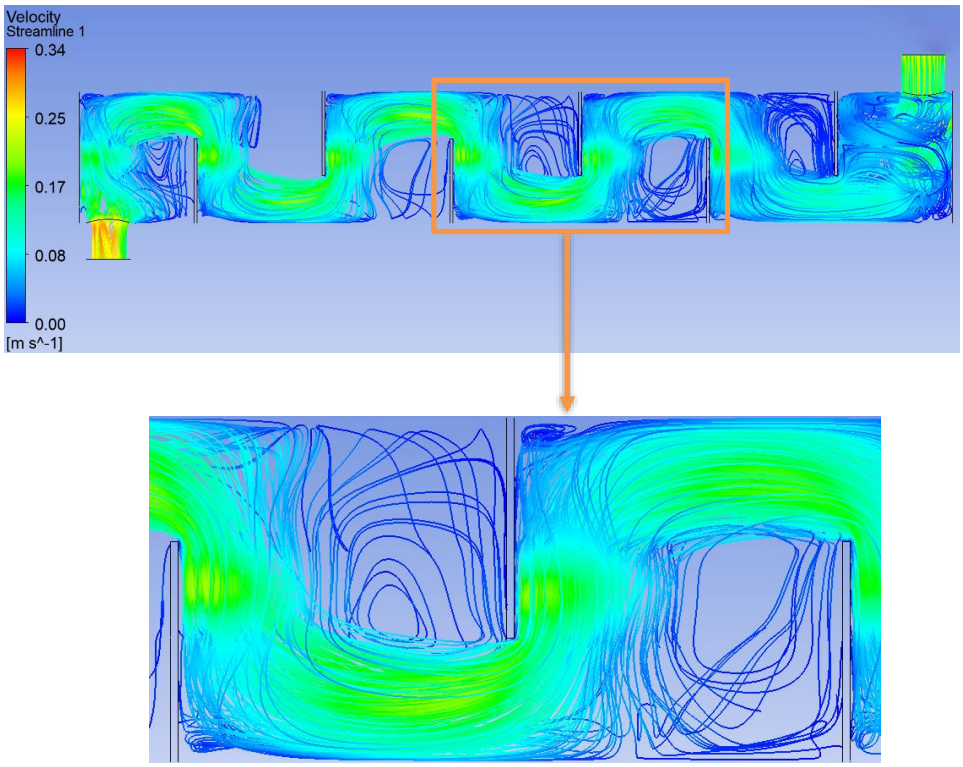
Velocity
Streamline 1
0.34
0.25
0.17
0.08
0.00
[m s^-1]

(b)

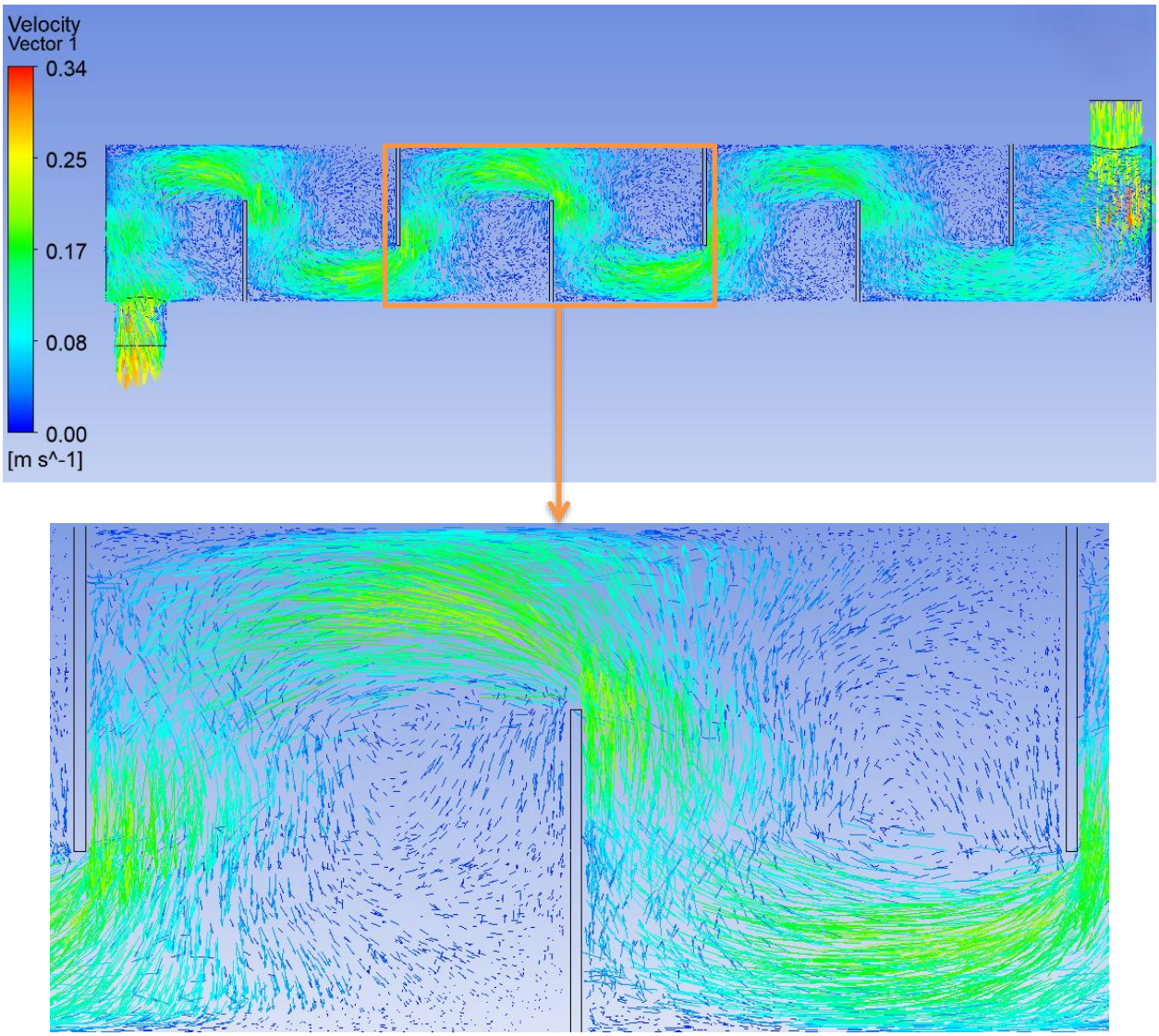

(c)

Fig. 15. Velocity-field visualization for Al_2O_3/water at ϕ=5% and Re=10000: (a) three-dimensional velocity streamlines, (b) YZ-plane velocity streamlines and (c) YZ-plane velocity vectors.

Velocity streamlines indicate a shell-side flow that is in a zigzag pattern due to the baffle layout. Vortices are separated near the baffles and recirculation regions are seen behind the baffle zones. The velocity-vector distribution also reveals lower velocity zones behind the baffles that are indicative of local recirculation zones. These flow features account for the pressure drop and mixing in the shell side.

4. Conclusion

The present study provides a systematic thermo-hydraulic comparison of water-based mono and binary hybrid nanofluids in a baffled shell-and-tube heat exchanger using a unified CFD framework. The numerical model was validated against benchmark shell-side data, showing maximum deviations of 0.42%, 3.06%, 7.20%, and 6.74% for outlet temperature, pressure drop, heat-transfer rate, and heat-transfer coefficient, respectively. The key results are outlined below:

- Increasing the Reynolds number from 10,000 to 25,000 enhanced the heat-transfer rate, heat-transfer coefficient, and average Nusselt number for all investigated working fluids. This improvement was associated with stronger shell-side mixing, intensified cross-flow around the tube bundle, and reduced thermal boundary-layer thickness. However, the pressure drop also increased, confirming a clear thermal–hydraulic trade-off.
- Increasing the nanoparticle volume fraction from 1% to 5% improved the heat-transfer rate and heat-transfer coefficient for both mono and binary hybrid nanofluids. In addition, the pressure drop also rose with the particle loading. At higher volume fraction, the average Nusselt number reduced due to the significant effect of the increase in the effective thermal conductivity on the Nusselt number formulation despite the increase in the heat transfer coefficient.
- Among the single nanofluids, GNP/water exhibited the strongest thermal performance, with the highest heat-transfer-rate enhancement of 10.44% at $\phi = 5\%$ relative to pure water. However, this improvement was accompanied by a comparatively higher pressure-drop tendency. ZnO/water exhibited the best hydraulic performance and Al_2O_3/water exhibited an intermediate thermal–hydraulic performance.
- Among the binary hybrid nanofluids, Al_2O_3–GNP/water achieved the highest heat-transfer-rate enhancement of 9.49% at $\phi = 5\%$, followed by ZnO–GNP/water and Al_2O_3–ZnO/water with enhancements of 8.29% and 7.07%, respectively.This indicates that with the addition of GNP thermal performance is enhanced but so is the hydraulic resistance.
- The mass-flow-rate analysis revealed trends similar to those of the Reynolds-number

analysis. Increasing the shell-side mass flow rate increased both the heat-transfer rate and pressure drop, but decreased the outlet temperature.Thus, higher flow intensity improves thermal performance, but the associated pressure-drop penalty should be carefully considered.

- The pressure, temperature and velocity-field visualizations corroborated the quantitative results. The baffle-induced zigzag flow, recirculation zones, and flow separation promoted shell-side mixing and heat transfer, while also increasing hydraulic resistance.

Overall, GNP-containing fluids are more suitable when maximum heat-transfer enhancement is the main objective, whereas ZnO/water and Al_2O_3–ZnO/water may be preferable when lower pressure drop and reduced pumping-power demand are prioritized. Therefore, no single nanofluid can be considered optimal for all operating conditions, and the selection of working fluid should depend on the required balance between thermal enhancement and hydraulic penalty. Future studies should consider two-phase modelling, nanoparticle stability, pumping-power analysis, entropy-generation evaluation, and experimental validation to support practical implementation in compact STHE systems.

Funding Declaration: The authors received no financial support for the research, authorship, and/or publication of this article.

Ethics, Consent to Participate, and Consent to Publish declarations: not applicable.

References

1. Marzouk, S.A.; Abou Al-Sood, M.M.; El-Said, E.M.S.; Younes, M.M.; El-Fakharany, M.K. A Comprehensive Review of Methods of Heat Transfer Enhancement in Shell and Tube Heat Exchangers. *J Therm Anal Calorim* **2023**, *148*, 7539–7578, doi:10.1007/s10973-023-12265-3.
2. Chen, L.-Y.; Adi, V.S.K.; Laxmidewi, R. Shell and Tube Heat Exchanger Flexible Design Strategy for Process Operability. *Case Studies in Thermal Engineering* **2022**, *37*, 102163, doi:10.1016/j.csite.2022.102163.

3. Hossein Zolfagharnasab, M.; Zamani Pedram, M.; Hoseinzadeh, S.; Vafai, K. Application of Porous-Embedded Shell and Tube Heat Exchangers for the Waste Heat Recovery Systems. *Applied Thermal Engineering* **2022**, *211*, 118452, doi:10.1016/j.applthermaleng.2022.118452.
4. Hasan, S.M.; Iqbal, S.; Khan, I.; Javaid, A.; Sajid, M. Performance Enhancement of a Shell-and-Tube Heat Exchanger Using a Novel Baffle Design. *Case Studies in Thermal Engineering* **2025**, *74*, 106800, doi:10.1016/j.csite.2025.106800.
5. Chen, J.; Li, N.; Ding, Y.; Klemeš, J.J.; Varbanov, P.S.; Wang, Q.; Zeng, M. Experimental Thermal-Hydraulic Performances of Heat Exchangers with Different Baffle Patterns. *Energy* **2020**, *205*, 118066, doi:10.1016/j.energy.2020.118066.
6. Khoi Hoang, H.M.; Cao, H.-L.; Quang Pham, P.M.; Hajjar, A.; Nguyen, V.L. A Novel Shell-and-Tube Heat Exchanger Design with Alternative Inclined Baffles. *Case Studies in Thermal Engineering* **2025**, *65*, 105542, doi:10.1016/j.csite.2024.105542.
7. Biçer, N.; Engin, T.; Yaşar, H.; Büyükkaya, E.; Aydın, A.; Topuz, A. Design Optimization of a Shell-and-Tube Heat Exchanger with Novel Three-Zonal Baffle by Using CFD and Taguchi Method. *International Journal of Thermal Sciences* **2020**, *155*, 106417, doi:10.1016/j.ijthermalsci.2020.106417.
8. Rehman, T.; Park, C.W. Advances in Nanofluids for Tubular Heat Exchangers: Thermal Performance, Environmental Effects, Economics and Outlook. *Energy* **2024**, *308*, 132732, doi:10.1016/j.energy.2024.132732.
9. Rahman, M.A.; Hasnain, S.M.; Pandey, S.; Tapalova, A.; Akylbekov, N.; Zairov, R. Review on Nanofluids: Preparation, Properties, Stability, and Thermal Performance Augmentation in Heat Transfer Applications. *ACS omega* **2024**, *9*, 32328–32349.
10. Porgar, S.; Huminic, G.; Huminic, A.; Najibolashrafi, R.; Salehfekr, S. Application of Nanofluids in Heat Exchangers-A State-of-the-Art Review. *International Journal of Thermofluids* **2024**, *24*, 100945.
11. Wang, Y.; Peng, Y.; Tao, Y.; Shi, L.; Liu, Q.; Ma, Y.; Tu, J.; Liu, X. Evaluation Methods of Thermo-Hydraulic Performance in Nanofluids: A Comprehensive Review. *Applied Thermal Engineering* **2024**, *240*, 121989, doi:10.1016/j.applthermaleng.2023.121989.
12. Rafid, M.; Azad, A.; Prottoy, S.; Alam, S.; Rahman, M.; Miah, M.J.; Hossain, M.S.; Rahman, M. Augmentation of Heat Exchanger Performance with Hybrid Nanofluids: Identifying

Research Gaps and Future Indications-A Review. *International Communications in Heat and Mass Transfer* **2024**, *155*, 107537.

13. Huminic, G.; Huminic, A. Hybrid Nanofluids for Heat Transfer Applications–a State-of-the-Art Review. *International Journal of Heat and Mass Transfer* **2018**, *125*, 82–103.
14. Sarkar, J.; Ghosh, P.; Adil, A. A Review on Hybrid Nanofluids: Recent Research, Development and Applications. *Renewable and Sustainable Energy Reviews* **2015**, *43*, 164–177.
15. Babar, H.; Ali, H.M. Towards Hybrid Nanofluids: Preparation, Thermophysical Properties, Applications, and Challenges. *Journal of Molecular Liquids* **2019**, *281*, 598–633.
16. Farajollahi, B.; Etemad, S.G.; Hojjat, M. Heat Transfer of Nanofluids in a Shell and Tube Heat Exchanger. *International Journal of Heat and Mass Transfer* **2010**, *53*, 12–17.
17. Lotfi, R.; Rashidi, A.M.; Amrollahi, A. Experimental Study on the Heat Transfer Enhancement of MWNT-Water Nanofluid in a Shell and Tube Heat Exchanger. *International Communications in Heat and Mass Transfer* **2012**, *39*, 108–111, doi:10.1016/j.icheatmasstransfer.2011.10.002.
18. Ahmadi, M.R.; Toghraie, D. Numerical Analysis of Flow and Heat Transfer in a Shell and Tube Heat Exchanger in the Gas Recirculation Cooling System of a Diesel Engine and the Effect of Nanofluid on Its Performance: MR Ahmadi et Al. *Journal of Thermal Analysis and Calorimetry* **2022**, *147*, 4853–4871.
19. Heydari, A.; Shateri, M.; Sanjari, S. Numerical Analysis of a Small Size Baffled Shell-and-Tube Heat Exchanger Using Different Nano-Fluids. *Heat Transfer Engineering* **2018**, *39*, 141–153, doi:10.1080/01457632.2017.1288052.
20. Hassaan, A.M. An Investigation for the Performance of the Using of Nanofluids in Shell and Tube Heat Exchanger. *International Journal of Thermal Sciences* **2022**, *177*, 107569, doi:10.1016/j.ijthermalsci.2022.107569.
21. Said, Z.; Rahman, S.M.A.; El Haj Assad, M.; Alami, A.H. Heat Transfer Enhancement and Life Cycle Analysis of a Shell-and-Tube Heat Exchanger Using Stable CuO/Water Nanofluid. *Sustainable Energy Technologies and Assessments* **2019**, *31*, 306–317, doi:10.1016/j.seta.2018.12.020.
22. Somasekhar, K.; Malleswara Rao, K.N.D.; Sankararao, V.; Mohammed, R.; Veerendra, M.; Venkateswararao, T. A CFD Investigation of Heat Transfer Enhancement of Shell and Tube

Heat Exchanger Using Al2o3-Water Nanofluid. *Materials Today: Proceedings* **2018**, *5*, 1057–1062, doi:10.1016/j.matpr.2017.11.182.

23. Kumar, N.; Sonawane, S.S. Experimental Study of Fe2O3/Water and Fe2O3/Ethylene Glycol Nanofluid Heat Transfer Enhancement in a Shell and Tube Heat Exchanger. *International Communications in Heat and Mass Transfer* **2016**, *78*, 277–284, doi:10.1016/j.icheatmasstransfer.2016.09.009.
24. Akhtari, M.; Haghshenasfard, M.; Talaie, M.R. Numerical and Experimental Investigation of Heat Transfer of α-Al_2O_3 /Water Nanofluid in Double Pipe and Shell and Tube Heat Exchangers. *Numerical Heat Transfer, Part A: Applications* **2013**, *63*, 941–958, doi:10.1080/10407782.2013.772855.
25. Muneeshwaran, M.; Srinivasan, G.; Muthukumar, P.; Wang, C.-C. Role of Hybrid-Nanofluid in Heat Transfer Enhancement – A Review. *International Communications in Heat and Mass Transfer* **2021**, *125*, 105341, doi:10.1016/j.icheatmasstransfer.2021.105341.
26. Vallejo, J.P.; Prado, J.I.; Lugo, L. Hybrid or Mono Nanofluids for Convective Heat Transfer Applications. A Critical Review of Experimental Research. *Applied Thermal Engineering* **2022**, *203*, 117926, doi:10.1016/j.applthermaleng.2021.117926.
27. Singh, B.; Sood, S. Hybrid Nanofluids Preparation, Thermo-Physical Properties, and Applications: A Review. *Hybrid Advances* **2024**, *6*, 100192, doi:10.1016/j.hybadv.2024.100192.
28. Malika, M.; Bhad, R.; Sonawane, S.S. ANSYS Simulation Study of a Low Volume Fraction CuO–ZnO/Water Hybrid Nanofluid in a Shell and Tube Heat Exchanger. *Journal of the Indian Chemical Society* **2021**, *98*, 100200, doi:10.1016/j.jics.2021.100200.
29. Behera, M.; Nayak, J.; Bal, S. Heat Transfer Analysis of CuO-ZnO/Water Hybrid Nanofluid in a Shell and Tube Heat Exchanger with Various Tube Shapes. *International Journal of Thermofluids* **2024**, *24*, 100972, doi:10.1016/j.ijft.2024.100972.
30. Shahsavar Goldanlou, A.; Sepehrirad, M.; Papi, M.; Hussein, A.K.; Afrand, M.; Rostami, S. Heat Transfer of Hybrid Nanofluid in a Shell and Tube Heat Exchanger Equipped with Blade-Shape Turbulators. *J Therm Anal Calorim* **2021**, *143*, 1689–1700, doi:10.1007/s10973-020-09893-4.

31. Alazwari, M.A.; Safaei, M.R. Combination Effect of Baffle Arrangement and Hybrid Nanofluid on Thermal Performance of a Shell and Tube Heat Exchanger Using 3-D Homogeneous Mixture Model. *Mathematics* **2021**, *9*, 881, doi:10.3390/math9080881.
32. Bouselsal, M.; Mebarek-Oudina, F.; Biswas, N.; Ismail, A.A.I. Heat Transfer Enhancement Using Al2O3-MWCNT Hybrid-Nanofluid inside a Tube/Shell Heat Exchanger with Different Tube Shapes. *Micromachines* **2023**, *14*, 1072, doi:10.3390/mi14051072.
33. Ghazanfari, V.; Imani, M.; Shadman, M.M.; Amini, Y.; Zahakifar, F. Numerical Study on the Thermal Performance of the Shell and Tube Heat Exchanger Using Twisted Tubes and Al2O3 Nanoparticles. *Progress in Nuclear Energy* **2023**, *155*, 104526, doi:10.1016/j.pnucene.2022.104526.
34. Mellal, M.; Benzeguir, R.; Sahel, D.; Ameur, H. Hydro-Thermal Shell-Side Performance Evaluation of a Shell and Tube Heat Exchanger under Different Baffle Arrangement and Orientation. *International Journal of Thermal Sciences* **2017**, *121*, 138–149, doi:10.1016/j.ijthermalsci.2017.07.011.
35. Ozden, E.; Tari, I. Shell Side CFD Analysis of a Small Shell-and-Tube Heat Exchanger. *Energy Conversion and Management* **2010**, *51*, 1004–1014, doi:10.1016/j.enconman.2009.12.003.
36. Versteeg, H.K. *An Introduction to Computational Fluid Dynamics the Finite Volume Method, 2/E*; Pearson Education India, 2007; ISBN 81-317-2048-9.
37. ANSYS, Inc. *Ansys Fluent Theory Guide*; ANSYS Help Documentation: Canonsburg, PA, USA, 2024;
38. Cheng, J.; Cheng, W.; Lin, W.; Yu, J. Heat Transfer Performance and Flow Characteristics of Helical Baffle–Corrugated Tube Heat Exchanger. *Applied Sciences* **2024**, *14*, 8905, doi:10.3390/app14198905.
39. Shih, T.-H.; Liou, W.W.; Shabbir, A.; Yang, Z.; Zhu, J. A New K-ϵ Eddy Viscosity Model for High Reynolds Number Turbulent Flows. *Computers & fluids* **1995**, *24*, 227–238.
40. Velagapudi, V.; Konijeti, K.R.; Aduru, K.S.C. Empirical Correlations to Predict Thermophysical and Heat Transfer Characteristics of Nanofluids. *Thermal Science* **2008**, *12*, 27–37.
41. Hussien, A.A.; Yusop, N.M.; Al-Nimr, M.A.; Abdullah, M.Z.; Janvekar, A.A.; Elnaggar, M.H. Numerical Study of Heat Transfer Enhancement Using Al2O3–Graphene/Water Hybrid

Nanofluid Flow in Mini Tubes. *Iran J Sci Technol Trans Sci* **2019**, *43*, 1989–2000, doi:10.1007/s40995-018-0670-1.

42. Ghasemi, B.; Aminossadati, S.M. Periodic Natural Convection in a Nanofluid-Filled Enclosure with Oscillating Heat Flux. *International Journal of Thermal Sciences* **2010**, *49*, 1–9, doi:10.1016/j.ijthermalsci.2009.07.020.
43. Hamilton, R.L.; Crosser, O.K. Thermal Conductivity of Heterogeneous Two-Component Systems. *Ind. Eng. Chem. Fund.* **1962**, *1*, 187–191, doi:10.1021/i160003a005.
44. Batchelor, G.K. The Effect of Brownian Motion on the Bulk Stress in a Suspension of Spherical Particles. *Journal of fluid mechanics* **1977**, *83*, 97–117.
45. Takabi, B.; Salehi, S. Augmentation of the Heat Transfer Performance of a Sinusoidal Corrugated Enclosure by Employing Hybrid Nanofluid. *Advances in Mechanical Engineering* **2014**, *6*, 147059.
46. Pak, B.C.; Cho, Y.I. HYDRODYNAMIC AND HEAT TRANSFER STUDY OF DISPERSED FLUIDS WITH SUBMICRON METALLIC OXIDE PARTICLES. *Experimental Heat Transfer* **1998**, *11*, 151–170, doi:10.1080/08916159808946559.
47. Maxwell, J.C. *A Treatise on Electricity and Magnetism*; Clarendon press, 1873; Vol. 1;.
48. Brinkman, H.C. The Viscosity of Concentrated Suspensions and Solutions. *Journal of chemical physics* **1952**, *20*, 571–571.